Contents

1 Introduction

Particle physics aims to describe and combine all fundamental building blocks and forces of the universe (preferably into one grand unifying theory). While this goal has certainly not been reached yet, every discovery is bringing modern particle physics closer to its goal. The most tested and understood model as of today is the Standard Model of Particle Physics (SM) describing all known fundamental particles and most fundamental forces. A very important puzzle piece in probing the SM was the discovery of the Higgs boson at the LHC at CERN in 2012 [1], as a joined effort of the ATLAS and CMS experiments. The Higgs boson had been formerly predicted in 1964 by Peter W. Higgs [2], who received the Nobel Prize in Physics 2013 after the discovery was made. The existence of this particle was necessary in the SM to explain the phenomenon of symmetry breaking in the electroweak force, from which massive elementary particles obtain their mass [1].

The goal of this report is an introduction to ATLAS physics including the attempt at a determination of the W boson mass and searching for the Higgs boson using original ATLAS data. At first, Section 2 outlines basic theoretical principles including the Standard Model and the structure of the ATLAS experiment. Section 3 will cover four separate tasks, the graphical evaluation of particle interactions in the ATLAS detector using the ATLANTIS program, the calibration of the electromagnetic calorimeter, the measurement of the W mass and finally the search for the Higgs boson.

2 Theory

In this chapter a short introduction to the Standard Model of Particle Physics will be given. Thereafter the Large Hadron Collider (LHC) and especially the ATLAS detector will be described in detail concluded by a short passage concerning the Higgs boson.

2.1 The Standard Model of Particle Physics

The Standard Model of Particle Physics (SM) describes the known building blocks of our universe and is currently the best theory available describing most fundamental forces (strong, weak and electromagnetic force) and particles. The aim of particle physics is at the moment to find physics beyond the standard model and thus expand or adjust it.
The Standard Model of Particle Physics can be separated into different groups of particles, which can be seen in Figure 2.1. These particles can be categorised into Spin 1 and Spin 1/2 particles, namely vector bosons and fermions. This list in Figure 2.1 is only missing the Higgs boson, which is a Spin 0 particle and will be discussed in more detail in Section 2.5.
The interaction between the elementary particle fermions can be described through the exchange of vector bosons. Thus the photon is e.g. the carrier-particle of the electromagnetic force. While the leptons can exist freely, quarks cannot. They are bound in colour neutral states called hadrons (e.g. protons, neutrons). Colour neutral refers to the colour charge (red, green, blue) of quarks, to which gluons representing the strong interaction couple.

2.2 The LHC and the ATLAS Experiment

The Large Hadron Collider (LHC) is one of the biggest particle accelerators in the world. Situated at CERN in Geneva, Switzerland and with a circumference of 27 km, it accelerates and collides protons at a centre of mass energy of up to 14 TeV and an integrated luminosity of $100\,\mathrm{fb}^{-1}$ per year [3].
The ATLAS experiment (A Toroidal LHC ApparatuS) is one of four experiments of the LHC. It is a multipurpose particle detector combining various sub detectors. Its main components are

Leptons (Spin 1/2)				
Generation	Flavour		Electrical charge [e]	Mass [MeV]
First	$\mathbf{e}$	Electron	-1	0,511
	$\boldsymbol{\nu_e}$	Elektron-neutrino	0	$< 2\,\mathrm{eV}$
Second	$\boldsymbol{\mu}$	Muon	-1	105,66
	$\boldsymbol{\nu_\mu}$	Muon neutrino	0	$< 0,19\,\mathrm{MeV}$
Third	$\boldsymbol{\tau}$	τ lepton	-1	1776,99
	$\boldsymbol{\nu_\tau}$	τ lepton neutrino	0	$< 18,2\,\mathrm{MeV}$

Quarks (Spin 1/2)				
Generation	Flavour		Electrical charge [e]	Mass [MeV]
First	$\boldsymbol{u}$	Up	2/3	1,7-3,1
	$\boldsymbol{d}$	Down	-1/3	4,1-5,7
Second	$\boldsymbol{c}$	Charm	2/3	1290
	$\boldsymbol{s}$	Strange	-1/3	80-130
Third	$\boldsymbol{t}$	Top	2/3	172900
	$\boldsymbol{b}$	Bottom	-1/3	4190

Exchange particle (Spin 1)					
Interaction	Vector boson		Electrical charge [e]	Mass [GeV]	Range [m]
Electromagnetic	$\boldsymbol{\gamma}$	Photon	0	0	∞
Weak	$\boldsymbol{W^\pm}$	Charged boson	± 1	80.399	$< 10^{-15}$
	$\mathbf{Z}$	Neutral boson	0	91.188	
Strong	$\boldsymbol{g}$	8 gluons	0	0	$\approx 10^{-15}$

Figure 2.1: The particles of the SM and their forces. From [3]

the inner detector, the electromagnetic calorimeter (ECAL), the hadronic calorimeter (HCAL) and the muon spectrometer.

Geometry:
In order to describe trajectories within the detector, it is necessary to define the used coordinates. The Cartesian coordinate system lies such that the z-direction is parallel to the proton beam. The x-axis is oriented to the centre of the LHC acceleration ring and y-axis, perpendicular to x and z, points upwards. However, when talking about particle tracks these two quantities are used most of all: the azimuthal angle ϕ and the pseudorapidity η. ϕ lies within the x-y-plane and describes a rotation around the beam axis. η is deducted from the polar angle θ and is defined as

$$\eta = -\ln\left(\tan\left(\frac{\theta}{2}\right)\right). \tag{2.1}$$

It includes the angle from the y-axis within the z-y-plane and thus indicates how much a particle deviates from moving straight upwards along the y-axis in the detector.

The Cartesian components of the momentum can be expressed in terms of the transverse momentum p_T, η and ϕ in the following way [4]

$$\begin{aligned} p_x &= p_T \cos(\phi) \\ p_y &= p_T \sin(\phi) \\ p_z &= p_T \sinh(\eta). \end{aligned} \tag{2.2}$$

Inner Detector:
The inner detector consists of three different layers, see Figure 2.2. The first layer is a semiconductor tracker located directly around the beam pipe and is made of silicon pixels, hence the name Pixel detector (PD) for this first component. The innermost layer of the PD was especially designed to detect secondary vertices arising from jets of b-quarks. It is called insertable b-layer (IBM). After the PD follows the Semi-Conductor-Tracker (SCT), which is also made of silicon. Here, however, the detector is not divided in small pixels but into stripes. This allows for the covering a wider area. The outermost layer of the inner detector is the transition radiation tracker (TRT), which combines a straw tracker and a transition radiation detector. A straw tracker consists of several long tube-shaped drift tubes (straws) detecting particles via gas ionisation [5]. The transition radiation tracker works by using layers with different refractive indices. The transition radiation emitted by the particles when passing through the different layers is measured [5]. This allows the identification of electrons.

The main purpose of the inner detector in the ATLAS detector is the energy and trajectory measurement of charged particles. This is also done with the help of the superconducting solenoid magnet in which the inner detector is placed, enabling momentum measurement of charged particles.

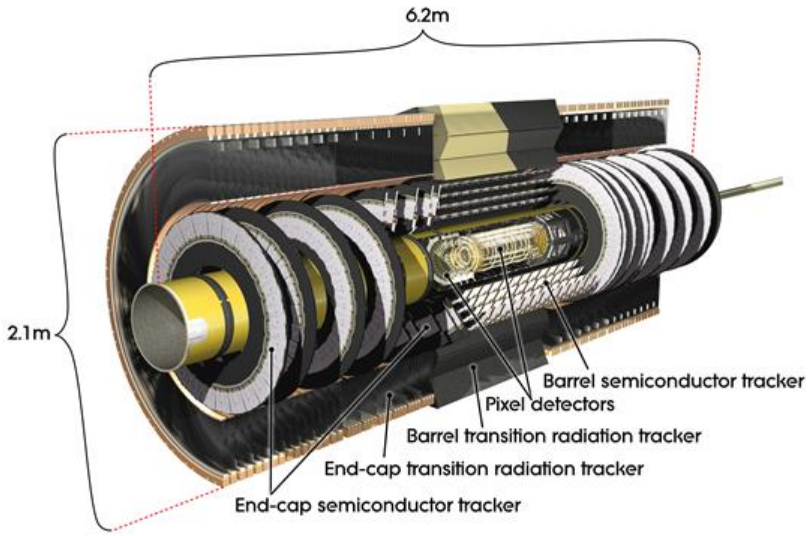

Figure 2.2: Depiction of the inner detector consisting of the pixel detector, the semi-conductor-tracker and the transition radiation tracker. Image from [6]

Electromagnetic Calorimeter:
The purpose of the electromagnetic calorimeter is the energy measurements and identification of particles that interact via the electromagnetic force, for instance electrons and photons.
It has a fine granularity and hence a good resolution. The calorimenter consists of alternating layers of lead as the absorber material and liquid argon as an active scintillating medium. Due to this structure, the particles form showers when crossing the calorimeter. The ECAL is built from three different layers, each with different cell shapes. The first layer has a very fine segmentation in η which allows a differentation between $\pi^0 \to \gamma\gamma$ decays and photons. Covering a

wider range, the other two layers have a coarser granularity and serve for the measurement of the energy deposits [7].

Hadronic Calorimeter:
The hadronic calorimeter mainly measures hadronic showers initiated by hadronic inelastic interaction with the active calorimeter material. The ATLAS HCAL is a sampling tile calorimeter. As can be seen in Figure 2.3, it is much larger than the electromagnetic calorimeter due to the larger length scale of hadronic showers in comparison to electromagnetic showers. The active material are tiles made of plastic scintillators intersected by steel absorber plates. In addition to the tile calorimeter there are also the calorimeter end caps, which again consist of liquid Argon as active material with intersecting copper tiles. It should be noted that the resolution is reduced in comparison to the ECAL, due to intrinsic effects of hadronic showers, which lead to additional fluctuations in the measured signal.

Muon Spectrometer:
The muon detectors, which can also be seen in Figure 2.3, consist of so-called muon chambers, which include different types of gas tracking detectors (e.g. resisitive plate chambers (RPCs)). Good momentum resolution of the muon system is guaranteed due to the accompanying superconducting toroid magnet system. As the name suggests the muon spectrometer measures minimum ionising muons passing through its active material and provides an accurate tracking of muons.

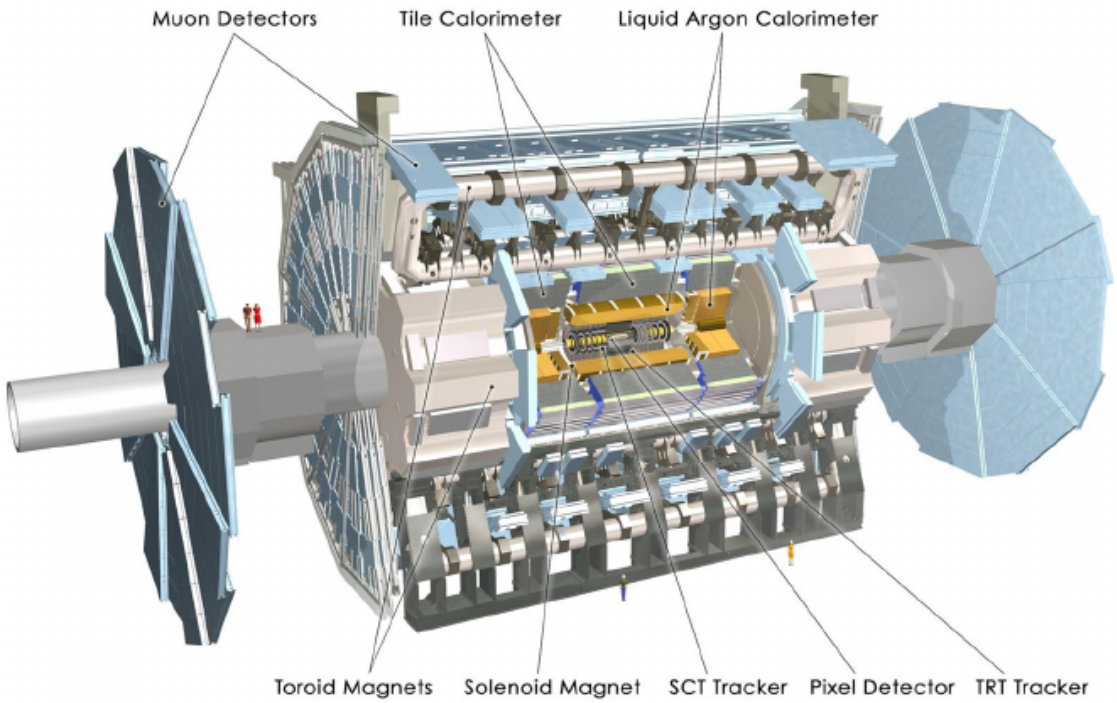

Figure 2.3: Schematic view of the ATLAS experiment. It is obvious that the hadronic calorimeter exceeds the size of the electromagnetic calorimeter in order to stop the deeper penetrating hadronic showers. Image from [8]

2.3 Particle Reconstruction

The above mentioned detector parts are used in various multipurpose detectors for so called particle reconstruction or particle identification. The information from the different detector parts are also used in Section 3.1 to reconstruct particle type and mass by looking at cross sections

of ATLAS events. Table 2.1 shows the different types of particles that can be measured/leave tracks in associated detector parts, in multipurpose detectors like ATLAS.

Particle Type	Inner Detector	ECAL	HCAL	Muon Detector
e	X	X		
γ		X		
μ				X
charged hadrons	X	X	X	
neutral hadrons			X	
ν				

Table 2.1: Different particles and the associated detector parts in which they mainly deposit their energy.

Charged/neutral hadrons that leave signatures in the detectors are e.g. π, K. Others like B hadrons have only a small range before decaying, thus they need to be reconstructed via their decay products. This is done via B tagging, where secondary vertices are detected.

The primary vertex of an interaction is the collision point of the two proton bunches circulating inside of the LHC, a secondary vertex is the vertex that can be reconstructed from secondary interaction/decay processes. For example: A B hadron produced in the collision decays within $\sim$ µm of the primary vertex into secondary particles. These have a longer lifetime and thus their tracks can be reconstructed using the inner tracker. Through data from the inner tracker, their origin can be reconstructed which does not lie on the same position as the proton bunch collision. The distance between primary and secondary vertex is then called the impact parameter.

Neutrinos cannot be detected directly by the detector parts due to their weak interaction with ordinary matter. However they can be reconstructed by the energy imbalance prevalent in the detector when examining all other measurable processes. Through this missing transverse energy E_T^{miss} they can be reconstructed using the polar and azimuthal angles:

$$E_x^{miss} = -\sum_i E_i sin(\theta_i) cos(\phi_i) \tag{2.3}$$

$$E_y^{miss} = -\sum_i E_i sin(\theta_i) sin(\phi_i) \tag{2.4}$$

$$E_T^{miss} = \sqrt{(E_x^{miss})^2 + (E_y^{miss})^2} \tag{2.5}$$

Other particles, which includes e.g. the τ lepton, Z or Higgs boson can only be reconstructed by their decay products.
The transverse energy is especially important in these types of experiment. Since the proton bunches collide with each other head on, most of the energy continues and is lost along the beam pipe. Thus not the total energy is of interest, but the energy in the transverse plane, which needs to be conserved.

2.4 Physics at the Terascale

There are some important parameters that are needed when working with high energy physics. Some of these will be sketched shortly:

Relativistic kinematics
Due to the nature of high energy physics it is important to consider relativistic kinematics for kinematic calculations. This means using four-vectors with natural units, e.g. for the position

and momentum:

$$x = \begin{pmatrix} ct \\ x \\ y \\ z \end{pmatrix}, \quad p = \begin{pmatrix} E \\ p_x \\ p_y \\ p_z \end{pmatrix} \tag{2.6}$$

Four vectors are conserved quantities, furthermore their scalar products are Lorentz invariant (invariant under Lorentz transformations). Thus it is preferable to use

$$\vec{E}^2 - \vec{p}^2 = m^2 \tag{2.7}$$

for energy/momentum calculations. This m is also called the invariant mass.

Scattering processes
In high energy scattering processes there are some important parameters that can be observed for different particles and interactions. A very important parameter is the cross section σ, which is a measure of probability of a certain physical process to occur. The larger the cross section, the more likely the process is to take place. It is intertwined with another important parameter: the luminosity L (in $[\mathrm{s}^{-1}\mathrm{cm}^{-2}]$). It solely depends on the experimental setup, in this case, the LHC. Also of interest is the integrated luminosity $\int L dt$ (in $[\mathrm{fb}^{-1}]$), integrated over the time for the experiment took place. These parameters are connected via

$$\sigma \cdot L = \dot{N} \tag{2.8}$$

where $\dot{N}$ is the counting rate of scattering processes per second.

Hadron collisions
The proton consists of a large number of partons and it is not the protons that collide with each other but the composite partons inside of them. It is then that hard scattering (scattering of actual elementary particles unlike the proton) Quantum Chromondynamics (QCD) processes take place (e.g. $q\bar{q} \to q\bar{q}, q\bar{q} \to gg$, etc.). Gluons involved in these QCD processes start fragmenting into hadronic jets, while colour charged remnants of the proton continue further on, until they also start to form jets along the beam line, which are usually not detectable. These high particle multiplicities sets hadron collisions apart from e.g. two-lepton interactions, since they usually produce final states with far fewer particles.

2.5 The Higgs Boson

In the aim of finding a gauge invariant theory for the weak force, symmetry conditions require massless Z and W gauge bosons. By this time in history, Z and W bosons with mass had already been discovered experimentally. However, through the extensive study and testing of quantum field theory it was discovered, that aforementioned massless gauge bosons could acquire their own mass by spontaneous symmetry breaking. The mechanism that gave rise to these mass terms is called the Higgs mechanism and further leads to the existence of another particle needed in the SM of Particle Physics: The Higgs boson.

The Higgs field (Φ was introduced, a complex scalar (spin 0) field as a carrier of the weak charge. This field gave rise to the so-called Higgs potential, the famous mexican-hat potential depicted in Figure 2.4:

$$V(\phi) = \mu^2|\phi|^2 + \lambda|\phi|^4 \tag{2.9}$$

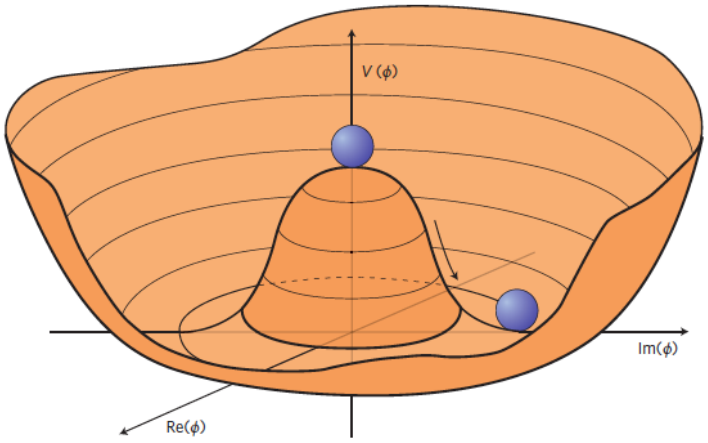

Figure 2.4: Illustration of the Higgs potential for $\mu^2 < 0$. Image from [9].

A negative factor μ^2, as in the illustration above, yields non-vanishing vacuum expectation values of Φ, which in turn yields for electroweak symmetry breaking. Expanding the Higgs field around the vacuum expectation value gives rise to mass terms for gauge boson. Furthermore, fermions can couple to the Higgs field, too, which gives rise to their masses as well. The Higgs field is a complex doublet with four degrees of freedom, one of which accounts for the Higgs particle itself. Kinematically, a Higgs boson can decay into any particles, which in sum are lighter than the Higgs mass. In collisions like the pp (or their partons) collisions at the LHC, Higgs bosons can be produced through the following mechanisms, which are depicted in Figure 2.5.

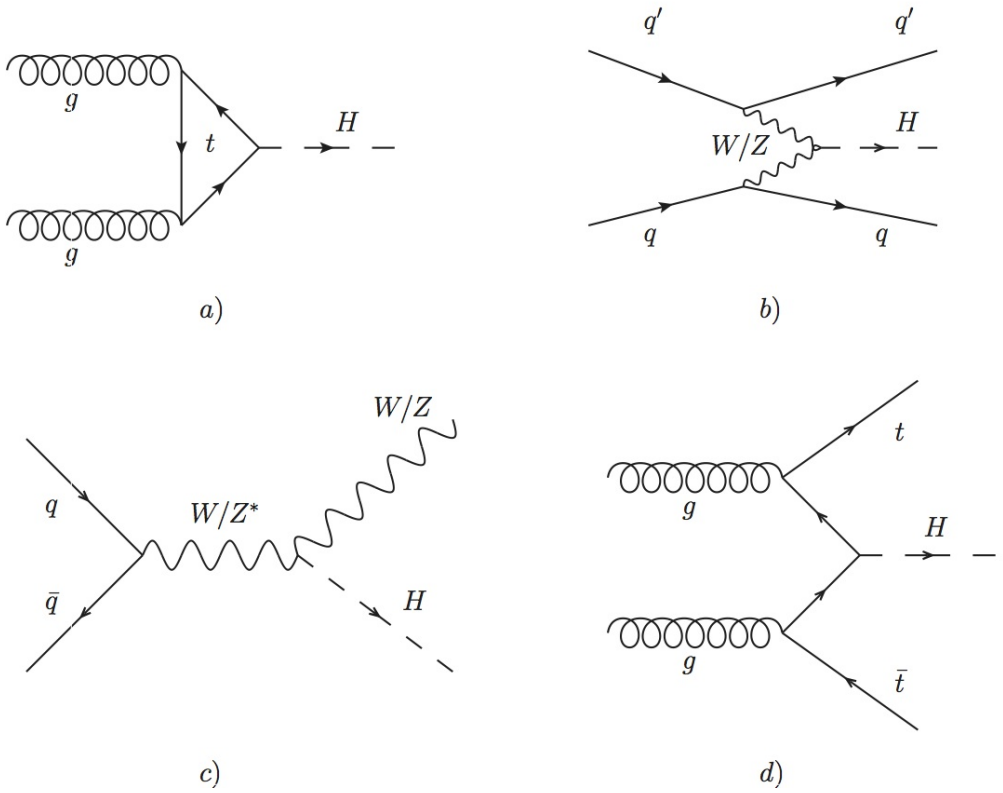

Figure 2.5: Production mechanisms of the Higgs boson at the LHC: a) gluon-gluon fusion b) WW or ZZ fusion c) W/Z Bremsstrahlung (vector boson associated production) d) $t\bar{t}$ fusion. From [10]

The combination of production mechanism and decay mechanism lead to a unique signature in the ATLAS detector. Thus, the search for the Higgs boson can be separated into distinct search channels based on production and decay mechanisms. The primary decay mechanisms of the Higgs boson are:

$$
\begin{aligned}
&H \to b\bar{b} \\
&H \to ZZ \to 4l \\
&H \to \tau^+\tau^- \\
&H \to W^+W^- \to 4q \\
&H \to gg
\end{aligned}
$$

Where $4l$ and $4q$ represent 4 leptons and 4 quarks respectively. For Higgs Physics at the LHC especially $H \to ZZ \to 4l$ is of interest, since it has a very clear signature in the detector in comparison with other lower lifetime decay products, which mostly decay into jets. Especially electrons and muons leave very distinct signatures in the detector, so $4e$, 4μ or $2e2\mu$ decays are very peculiar processes, which can also be seen in Section 3.1.

3 Methodology and Analysis

In this Section four different experimental analyses were conducted. At the beginning of each section the respective problem will be discussed and the methodology and results of the following analysis are outlined.

3.1 Graphical Evaluation of Particle Interactions with ATLANTIS

In this Section different particle interactions in the ATLAS detector are to be evaluated graphically with the ATLANTIS program, which displays three different viewing angles of events in the ATLAS detector. The graphical display shows the detectors response to different interactions and is furthermore able to graphically and numerically reconstruct particle trajectories, as well as various information on the transverse momentum p_T, the momentum p, the pseudorapidity η, the azimuthal angle ϕ and in some cases the missing transverse $E_{T,\text{Miss}}$ of each reconstructed particle.

When looking at the graphical display a hypothesis about the ongoing particle interaction can be made, this hypothesis can then be verified or tested via decay kinematic calculations.

In the following, six different event displays are considered. For each event the decay process is identified and either the invariant or at least the transverse mass of the original particle prior to the decay process is calculated.

Event 1

The first graphical display is depicted in Figure 3.2. On the left upper side, the x-y-plane of the detector is shown while the right upper side displays a cut in the η-ϕ-plane. The lower picture offers a side view of the detector along the x-axis on the z-y-plane. For determining the process, the profile of the x-y-plane is sufficient for the identification of the respective decay process.

In the first event, two muon tracks can be observed, which were identified due to the tracks left within the muon spectrometer. This directly indicates that the particle is a muon since they are the only charged particles reaching the outer part of the ATLAS detector.
These two muons might originate from a Z-boson. Thus the assumed decay process would be

$$Z \rightarrow \mu^+\mu^-.$$

A possible Feynman diagram of the supposed process can also be seen in Figure 3.1.

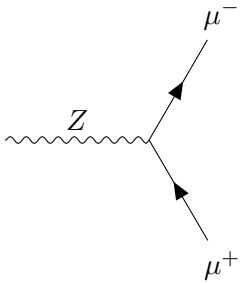

Figure 3.1: Possible Feynman diagram of event 1

In order to confirm this assumption, the invariant mass M of the two muons is calculated using

$$M = \sqrt{2m_\mu^2 + 2(E_1 \cdot E_2 - \vec{p}_1 \cdot \vec{p}_2)} = 91.2\,\text{GeV}$$

where E_1 and E_2 denote the energy of muon 1 and 2 and $\vec{p_1}$ and $\vec{p_2}$ name the respective momentum. $\vec{p_1}$ and $\vec{p_2}$ can be reconstructed from the variables η, ϕ and p_T using the equations in (2.2). This result validates the hypothesis of a Z-decay when comparing it to the mass listed in Figure 2.1.

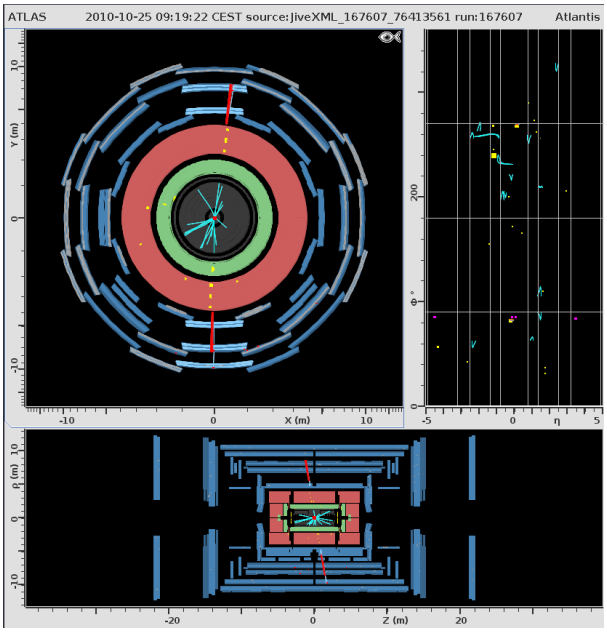

Figure 3.2: Event 1: The red lines on the outer edges of the detector (muon spectrometer) clearly call for the presence of muons.

Event 2

The second event can be found in Figure 3.4. Here, only one crucial track is visible, namely one of a muon that could be detected in the muon spectrometer. In addition, a photon was detected, which originates most likely from bremsstrahlung. Moreover, a certain amount of missing transverse energy $E_{T,\text{miss}}$ was observed, which stands for a neutrino being a product of the decay process. Thus, the original particle is expected to be a W boson and the stated decay is

$$W \to \mu + \nu_\mu.$$

In Figure 3.3, a possible Feynman diagram can be seen.

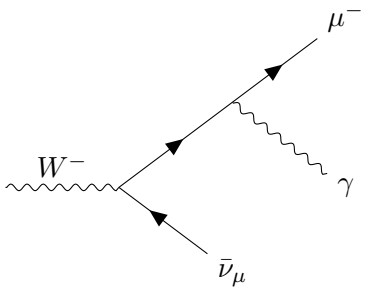

Figure 3.3: Possible Feynman diagram of event 2, of course charges could be inverse.

Again, this guess has to be verified by calculating the mass of the decayed particle. Unfortunately, since one of the involved particles is a neutrino, it is not possible to compute the

invariant mass of the supposed W boson. However, one can still calculate the transverse mass by only regarding the transverse kinematic components. By using the class `TLorentzVector` implemented in `ROOT`, a transverse mass of

$$M_T = 70.4\,\text{GeV}$$

was obtained. This result is smaller than the mass of the W-boson, which makes sense because only the transversal part of the mass was considered. Yet the mass is close enough to the W mass to most likely verify the stated process.

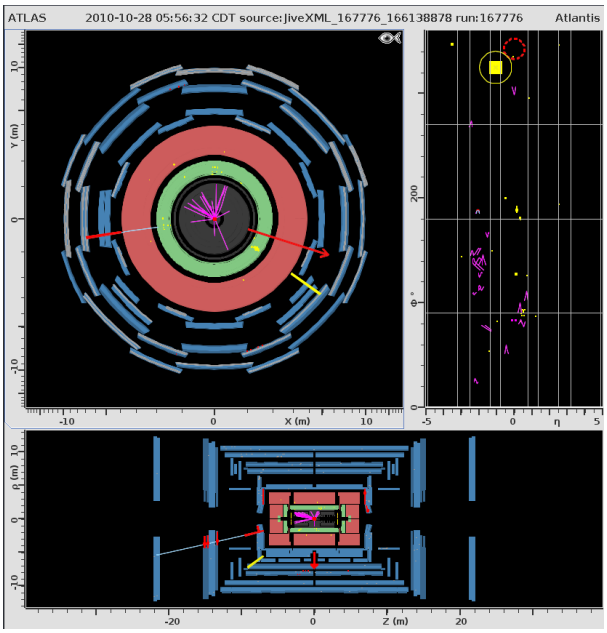

Figure 3.4: Event 2: The red arrow indicates missing transverse energy and hence is an evidence for neutrinos.

Event 3

The third event, see Figure 3.6, displays tracks of two muons and two b-jets. The b-jets indicate bottom quarks. Moreover, there is some amount of missing transverse energy, which implies the involvement of neutrinos in the decay process. Thus, it stands to reason that this event shows the decay of a top quark pair, since only top quarks are heavy enough to produce bottom quarks:

$$t\bar{t} \to \mu^+\mu^-\, b\,\bar{b}\,\nu_\mu\,\overline{\nu}_\mu$$

A Feynman graph of this process can be seen in Figure 3.5:

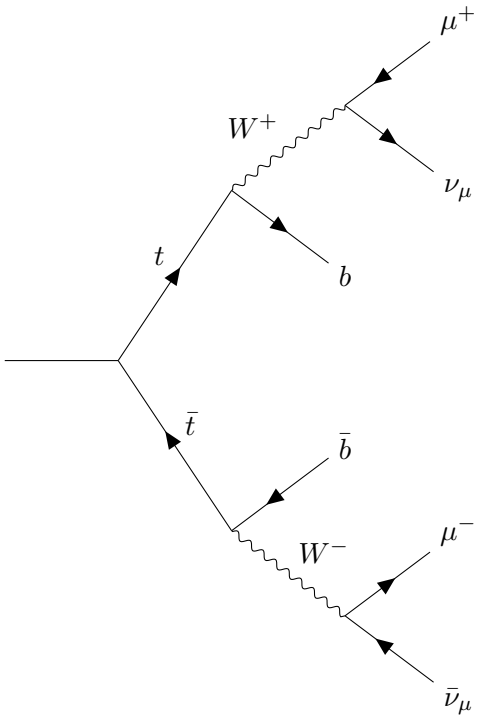

Figure 3.5: Possible Feynman diagram of event 3

As before, the transverse amount of mass can be computed due to the involvement of neutrinos. Additionally, one can try to find out which muon and which b quark originates from the same t quark. This is done by calculating the transverse mass of both possible combinations. The requirement, that the transverse mass of the muon and bottom together has to be smaller or equal to the mass of a top quark eliminates one combination. This procedure suggests that the muon on the lower left side belongs to the b-jet on the upper left side (top 1). Likewise, the muon and b quark on the lower right and upper right side originate from the same t (top 2).

With this knowledge, the respective shares of the missing transverse energy were added to both muon-bottom pairs and the transverse mass of both pairings was calculated to approximately

$$M_{T_1} = 171.6\,\mathrm{GeV} \quad \text{and} \quad M_{T_2} = 163.7\,\mathrm{GeV}.$$

Both resuls are smaller than the mass of a top quark and thus the assumption of the top decay is not falsified.

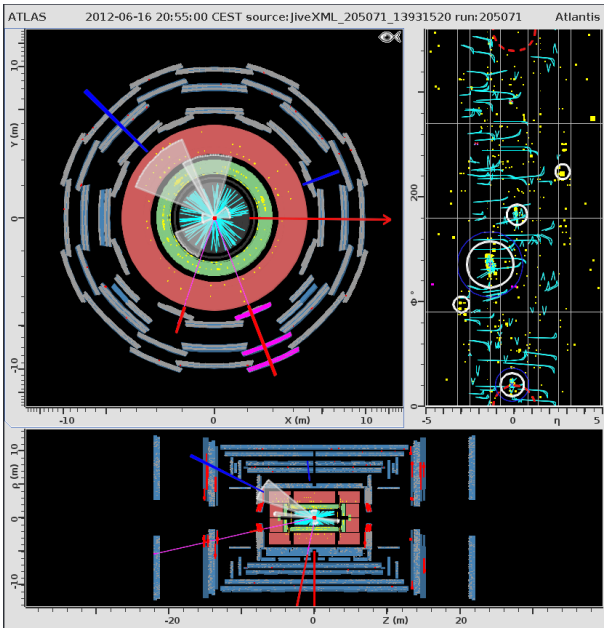

Figure 3.6: Event 3: The red arrow indicates missing transverse energy again. However, it is not necessarily just one missing particle involved. The translucent cones depict jets.

Event 4

Event 4, depicted in Figure 3.8, shows a similar signature as event 3, but with electrons instead of muons as leptons leaving their tracks in the ECAL:

$$t\bar{t} \rightarrow e^+e^-\, b\,\bar{b}\,\nu_e\,\overline{\nu}_e.$$

A Feynman graph of this process can be seen in Figure 3.7

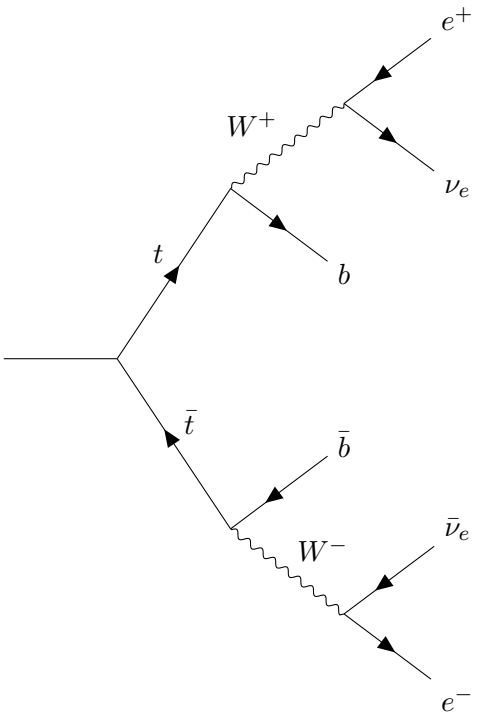

Figure 3.7: Possible Feynman diagram of event 4

Thus, the same approach as before is used, which hints that the lower electron comes from the same top as the b-jet on the left side (top 1) and that the upper electron and right b-quark belong together (top 2).
Again, after including the neutrinos' momentum, the calculation of both transverse masses leads to

$$M_{T_1} = 154.8\,\text{GeV} \quad \text{and} \quad M_{T_2} = 135.6\,\text{GeV}.$$

With this, the stated top quark pair decay can be validated, since both transverse masses lie below the mass of a top.

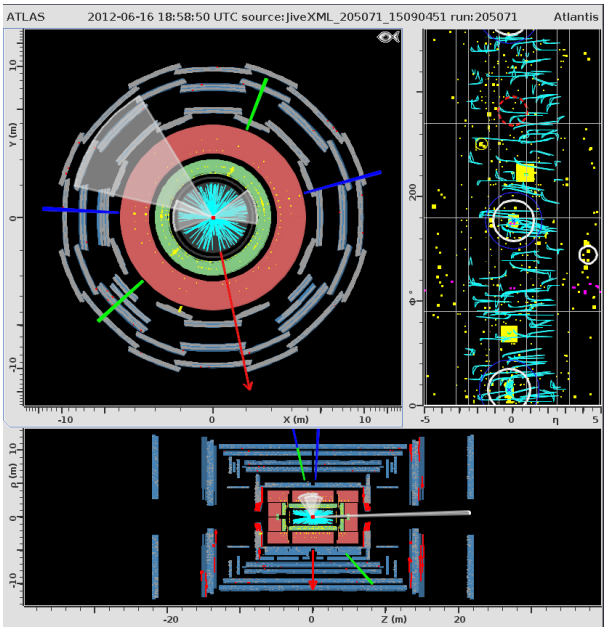

Figure 3.8: Event 4: Again the red arrow is hinting at missing transverse energy. The yellow depositions in the ECAL (green signature) hint at electrons for this process.

Event 5

The fifth event can be found in Figure 3.10. It shows four muon tracks and hence represents a possible Higgs candidate. The assumed decay process is a Higgs decaying into four muons with two Z bosons as an intermediate step:

$$H \to ZZ \to \mu^+\mu^-\mu^+\mu^-.$$

The Feynman graph of this process can be seen in Figure 3.9. The invariant mass of all four muons together yields

$$M = 120.7\,\text{GeV},$$

which approximately matches the mass of the Higgs boson.

Moreover, it can be guessed which muons originate from the same Z boson by calculating the invariant mass of all two-muon combinations. Since it is known, that for this decay process one of the Z bosons is virtual and one is real, the combinations where both invariant masses are too small for one Z boson to be real can be excluded. This requirement leaves only one possible combination, where the invariant masses are

$$M_{12} = 90.5\,\text{GeV} \quad \text{and} \quad M_{34} = 13.8\,\text{GeV}. \tag{3.1}$$

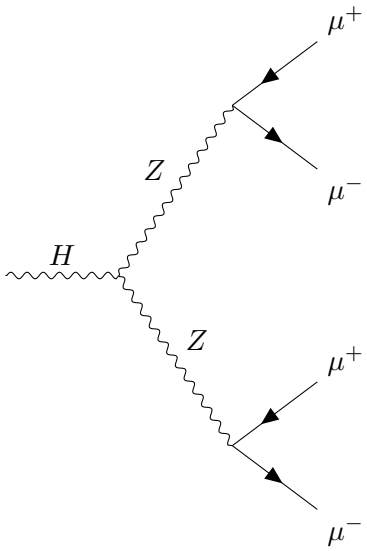

Figure 3.9: Possible Feynman diagram of event 5

M_{12} denotes the mass of the muon on the lower left side together with the upper muon and M_{34} stands for the invariant Mass of the two muons on the right side.

Because for all combinations of two muons, at most one Z boson was real respectively. It can therefore be excluded, that the observed decay products are from Z bosons created with ZZ pair production. This distinction will later be important in Section 3.4

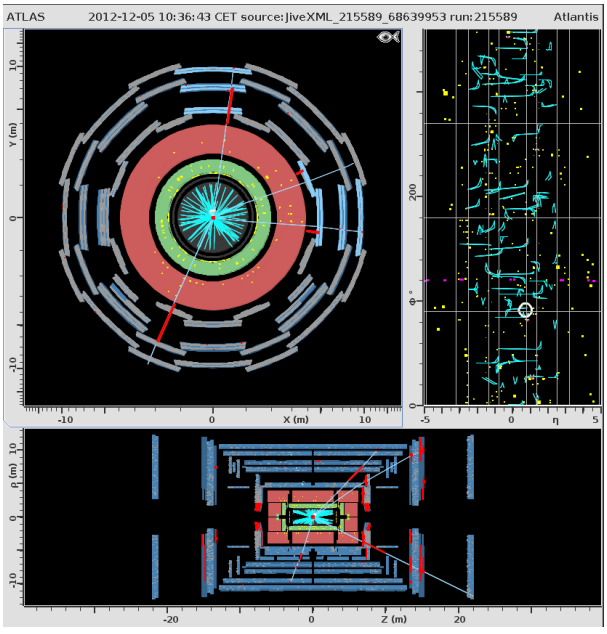

Figure 3.10: Event 5: The very distinct four muon signature of this Higgs decay.

Event 6

Similar to event 5, event 6 shows four lepton tracks, see Figure 3.12. This time, however, it involves two electrons and two muons. Thus, it might be the same decay channel as before in event 5, where a Higgs boson decays via two Z bosons into four leptons:

$$H \to ZZ \to e^+e^-\mu^+\mu^-.$$

A Feynman diagram of this process is shown in Figure 3.11.

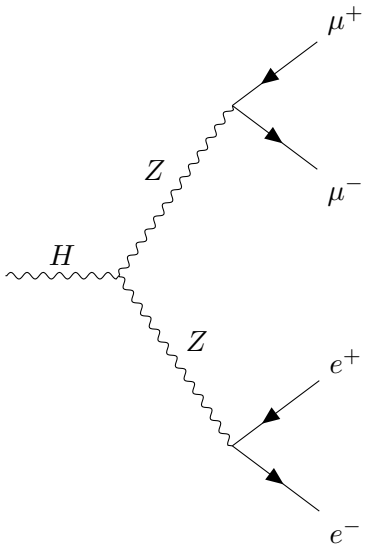

Figure 3.11: Possible Feynman diagram of event 6

Again, invariant mass using the contributions of all four leptons is of interest, which can be computed to

$$M = 125.5\,\text{GeV}.$$

This result corresponds to the mass of the standard model Higgs boson.

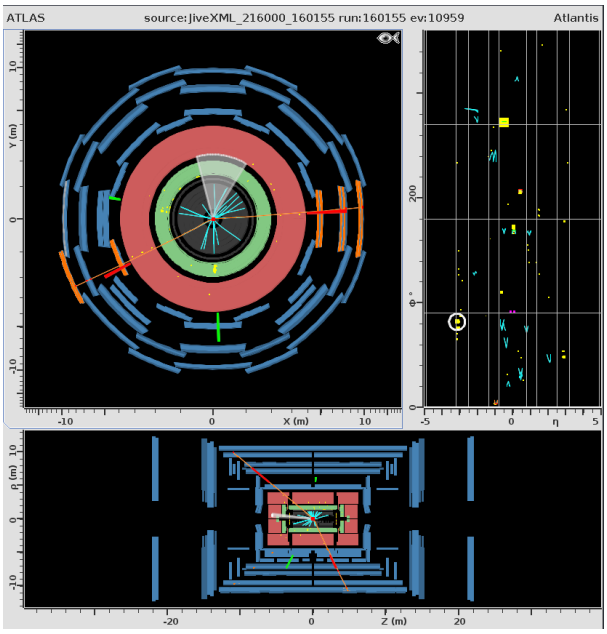

Figure 3.12: Event 6: This four lepton decay has a very distinct signature as well.

3.2 Calibration of the electromagnetic Calorimeter

The most relevant part of the ATLAS detector for measuring electrons is the electromagnetic calorimeter. There, the energy of the electrons is measured. However, when the electrons reach the ECAL, they already traversed the inner detector and consequently deposited a part of their energy there. Thus, the energy measured in the calorimeter does not correspond directly to the electron's energy due to the energy loss in the inner detector parts.

In order to solve this deviation, a calibration has to be performed. This can be achieved by the following parametrisation:

$$E_{\text{meas}} = E_{\text{true}}(1+\alpha),$$

where α is a calibration constant to be determined in this task.

For calibration, the following decay process is used:

$$pp \to Z \to e^+e^-.$$

This process has a large cross section and has been extensively studied. Moreover, the mass M_Z of the Z boson is known in the standard model and can hence be used for calibration.
The invariant mass M_{ee} of the two measured electrons is then fitted with a non-relativistic Breit-Wigner-function

$$f(M_{ee}) = \frac{\Gamma_Z^2/4}{(M_{ee}^2 - M_Z^2)^2 + \Gamma_Z^2/4}$$

with Γ_Z representing the decay width of the Z boson [3]. The fit yields the invariant mass of the two electrons. The calibration then aims at shifting the invariant mass of the two electrons towards the mass of the Z boson.

Before performing any calibration, the fit of the invariant mass of the two electrons results in

$$M_{ee} = 83.9\,\text{GeV}.$$

The according plot can be found in Figure 3.13.

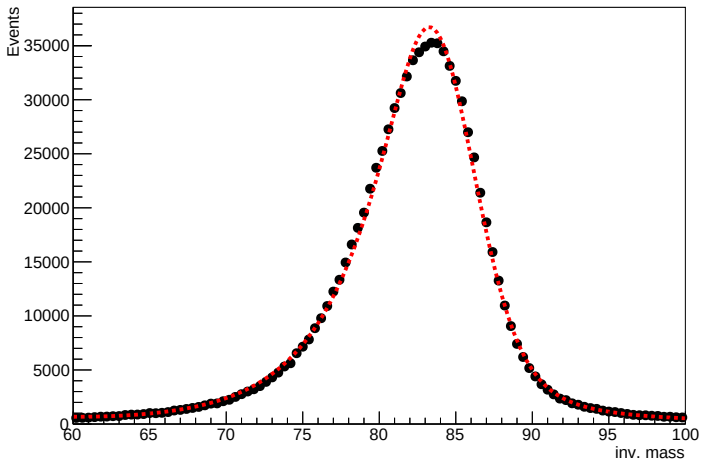

Figure 3.13: Invariant mass fit of the two electrons without calibration

For the calibration, the pseudorapidity η is considered foremost. The respective histogram is depicted in Figure 3.14. The number of measured events depends on the amount of material the electron had to traverse before reaching the calorimeter. Figure 3.15 shows the distribution of material depending on η. The more material the electron has to cross on its way, the smaller its energy when reaching the ECAL. Thus, there is a non-negligible dependency of the energy on the pseudorapidity, which is why η is used for the one-dimensional calibration. For η, a range from $0 \leq \eta \leq 2.47$ is selected since this is the pseudorapidity range covered by the inner detector.

Moreover, one can observe two distinct drops of the number of events at approximately $\eta = \pm 1.4$, where no events are measured. This can be explained by the detectors geometric structure. In this particular region of η, the calorimeter's end-caps meet the barrel part and in this area, due to the technical constraints, no measurement is possible.

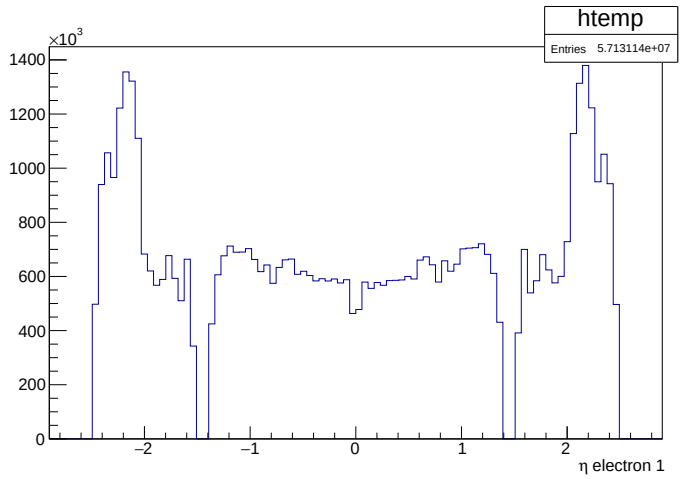

Figure 3.14: Histogram of the pseudorapidity η for electron 1.

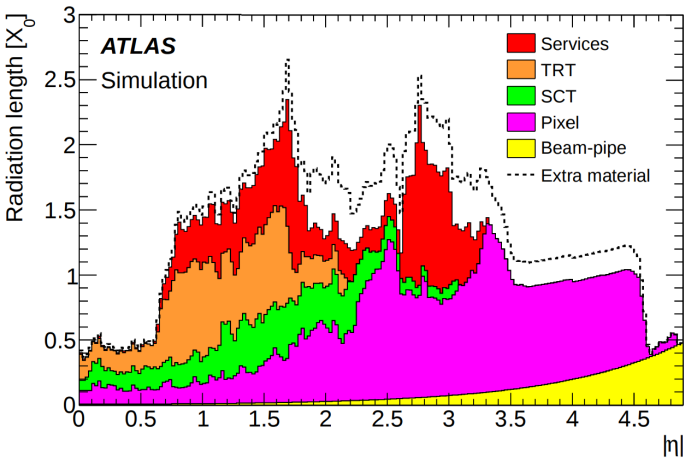

Figure 3.15: Material in the ATLAS detector traversed by a particle as a function of the pseudorapidity η. Picture taken from [11].

Performing the calibration in η yields the one-dimensional calibration factor α, depicted in Figure 3.16. The invariant mass of the two electrons after the calibration results in

$$M_{ee} = 90.5\,\text{GeV},$$

which is close to the mass of the Z boson of $M_Z = 91.2\,\text{GeV}$ (see Figure 2.1). The plot of the invariant mass including the Breit-Wigner function fit can be found in Figure 3.17.

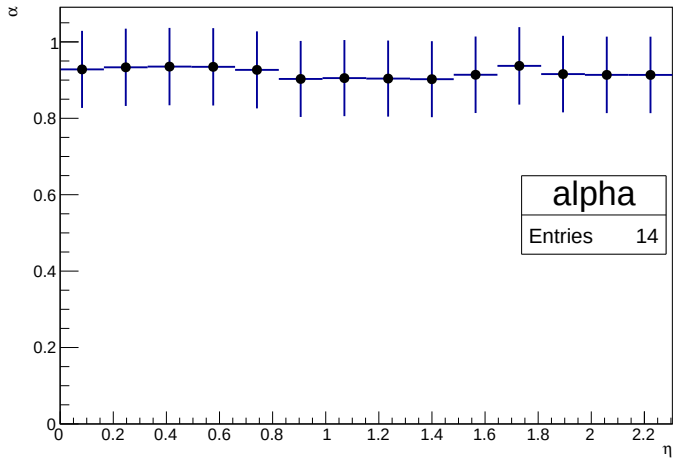

Figure 3.16: One-dimensional calibration factor α as a function of η

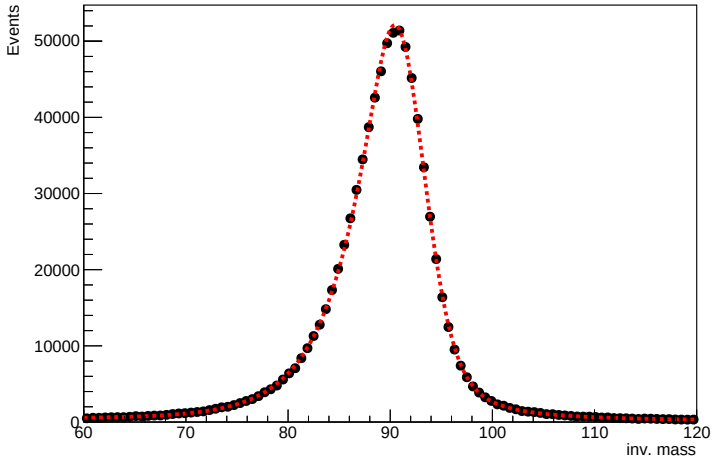

Figure 3.17: Invariant mass of the two electrons after performing the one-dimensional calibration

After executing the one-dimensional calibration, the influence of other possible parameters on the energy of the electrons measured in the ECAL is of interest. Therefore, the histogram of the azimuthal angel ϕ is considered next, see Figure 3.18. However, the measured number of events seems to be almost equally distributed. Moreover, the cylindrical symmetry of the ATLAS detector suggests, that the amount of material to be crossed does not differ for different angles ϕ. Consequently, this makes a calibration in ϕ unnecessary.

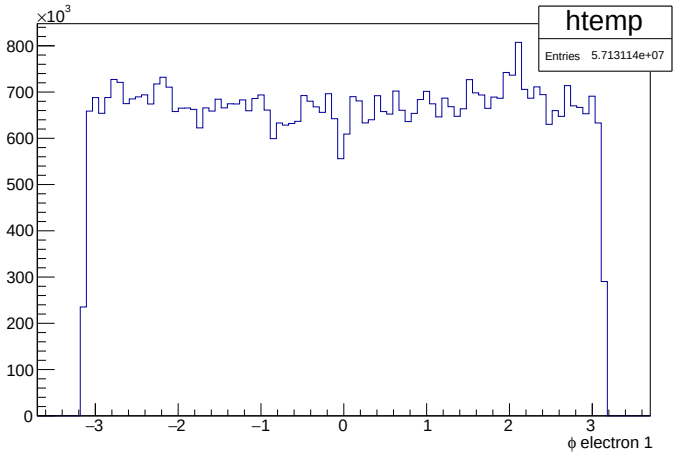

Figure 3.18: Histogram of the azimuthal angle ϕ for electron 1.

The transverse momentum on the other hand indicates a different characteristic. It is depicted in Figure 3.19. Electrons with a larger transverse momentum interact less, and thus they have a larger range and deposit less energy within the inner detector

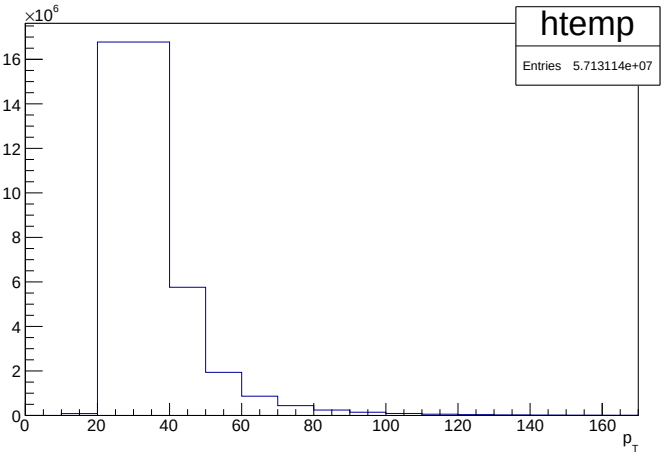

Figure 3.19: Histogram of the transverse momentum p_T of electron 1.

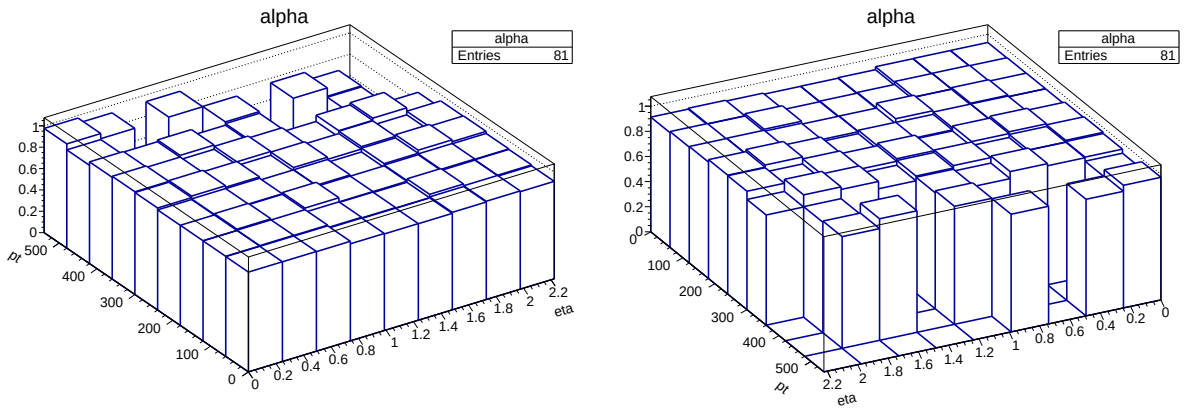

Figure 3.20: Plot of the two-dimensional calibration factor α depending on η and p_T.

Applying the two-dimensional calibration in η and p_T yields a transverse mass of

$$M_{ee} = 90.5\,\text{GeV}.$$

This result does not deviate from the invariant mass obtained from the calibration in one dimension. The corresponding fit can be seen in Figure 3.21.

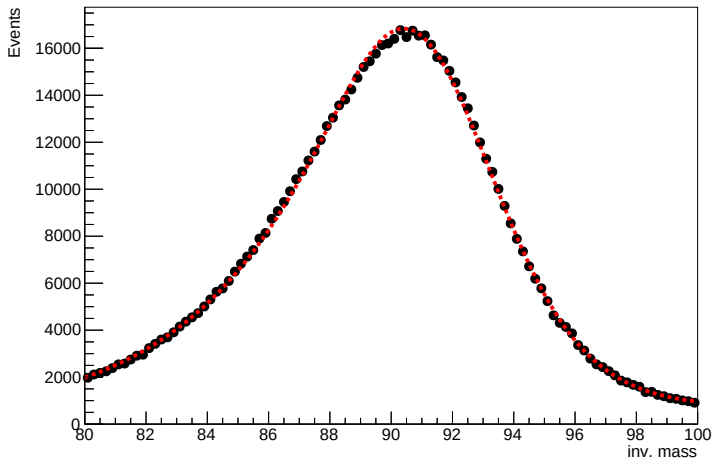

Figure 3.21: Invariant mass of the two electrons after performing the two-dimensional calibration in η and p_T

Since the two-dimensional calibration does not lead to a better result than the one-dimensional one and due to the time constraint of this one-week experiment, the next task was performed with the one-dimensional calibration.

3.3 Measurement of the W-mass

In this part the mass of the W boson was determined using the provided code skeletons `wmacro.C` and `Wmass.C`. Since the measurements precision is limited depending on the respective decay products, it is important to choose a convenient W decay channel for this. The branching ratios for the W decay are listed in Table 3.1.

Decay Process	Branching ratio [%]
$l\nu$	$\sim$10 (each τ, μ, e)
Jets	67

Table 3.1: Branching ratios for W decay [3].

Even though the decay through hadronic jets has a higher branching ratio, the mass measurement via the $W \to e\nu$ decay is much more precise (ECAL has a better resolution than HCAL), which is the decay that will be taken into account here. However, it should be noted that the neutrino will leave the detector unnoticed so the mass needs to be reconstructed through the transverse energy and momentum of the measured electron. This process corresponds to a two-body decay, which (in the rest frame of the W) means that both decay products have the same absolute value of momentum. This in turn, including some coordinate transformation, leads to the fact, that the transverse momentum of the daughter particles is peaked around $p_T = \frac{1}{2} m_W$ (when neglecting their mass). Thus, in order to find the W mass, histograms of the p_T distributions of the measured and simulated data will be generated. The peak at half-mass is called Jacobi peak, although as can be seen in this chapter, it is not a very sharp peak. It is smeared out, among other things, due to detector resolution and W decay width.

3.3.1 Weighting of the data set

With the help of the one-dimensional calibration conducted in Section 3.2, the W mass was determined from real ATLAS data using a simulated set of $W \to e\nu$ and background processes data.

These simulated data sets need to be weighted to different possible W masses, which will be helpful in determining the real W mass.
However there is not a single $W \to e\nu$ process, but the two distinct decays $W^+ \to e^+\nu_e$ and $W^- \to e^-\bar{\nu_e}$. Since they don't have identical cross sections, their respective data sets need to be scaled accordingly. In order to weigh the data to different possible masses the function `getWeights()` in `Wmass.C` is being used, which can read out a `root` file containing the invariant mass of W^+ and W^-. The invariant masses are scaled by a factor of

$$\frac{\sigma}{N} = \frac{1}{\int L dt} \tag{3.2}$$

equivalent to the inverse of their integrated luminosity (see Equation 2.8). Where N is the number of events in each data set, that can be, beside others, obtained from the respective data set via the root tree `truthTree`. The cross sections used for scaling are listed in Table 3.2.

Process	σ [nb]
$W^+ \to e^+\nu_e$	6.16
$W^- \to e^-\bar{\nu_e}$	4.30

Table 3.2: Cross sections of $W \to e\nu$ processes [3].

Then, a Breit Wigner function is fitted to the histogram of the W mass distribution. The Breit Wigner peak is then shifted to masses that can be specified. Of course these masses should be chosen close to and surrounding the expected W mass. From the previous and the shifted mass, weights are calculated. Two examples for these weighting factors, obtained through `getWeights()` can be seen in Figure 3.22. One is used for re-weighting a data set to a smaller mass and one induces a weighting to a larger mass than before.

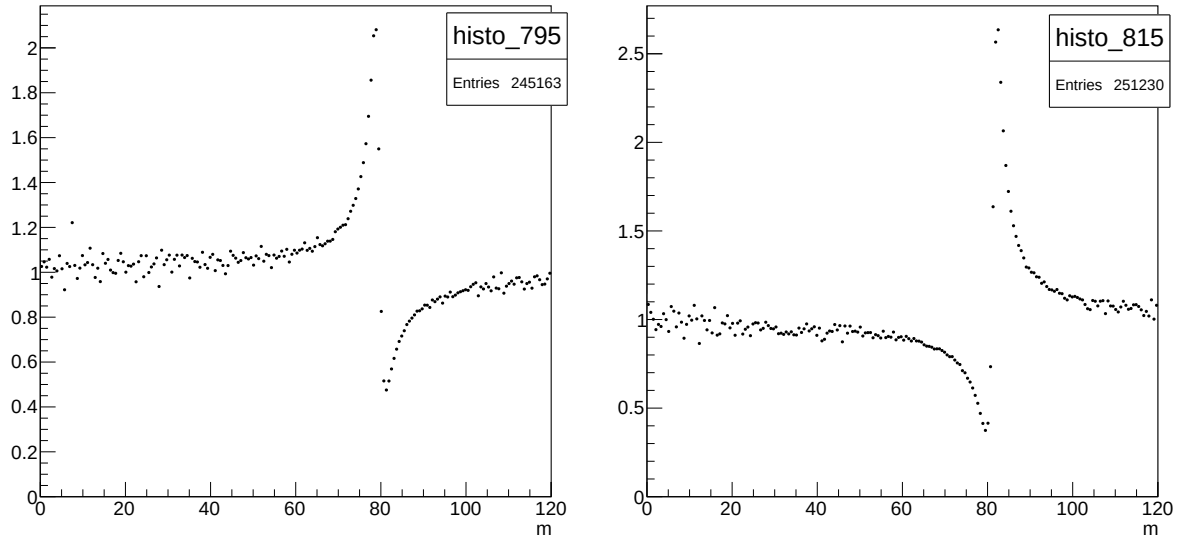

(a) weights for a mass of $m_W = 79.5\,\text{GeV}$ (b) weights for a mass of $m_W = 81.5\,\text{GeV}$

Figure 3.22: Two examples for the weighting factors used for re-weighting data sets to different m_W.

3.3.2 Determination of proper selection criteria

Next the simulated data (here weighted to $m_W = 80\,\text{GeV}$), background data and measured data are all taken into account. To reduce background from processes like

$$\begin{aligned} W &\to t\bar{t} \\ Z &\to e^+e^- \\ Z &\to \tau\bar{\tau} \\ W &\to \tau\nu, \end{aligned}$$

which could all be mistaken for $W \to e\nu$ processes under certain circumstances, selection criteria need to be identified. Even before looking at histograms of the data there are certain criteria the data needs to pass. A major background process is falsely identified electrons, which can be easily evaded by setting strict criteria for electron selection. Also, to prevent $Z \to e^+e^-$ from passing as W, the selection criterion, that two-electron events are suppressed, is crucial. These selections are incorporated into the following plots, which were generated using `wmacro.C`. The plot for the invariant mass after applying these selections and after applying the calibration from Section 3.2 to the measured data, can be seen in Figure 3.23.

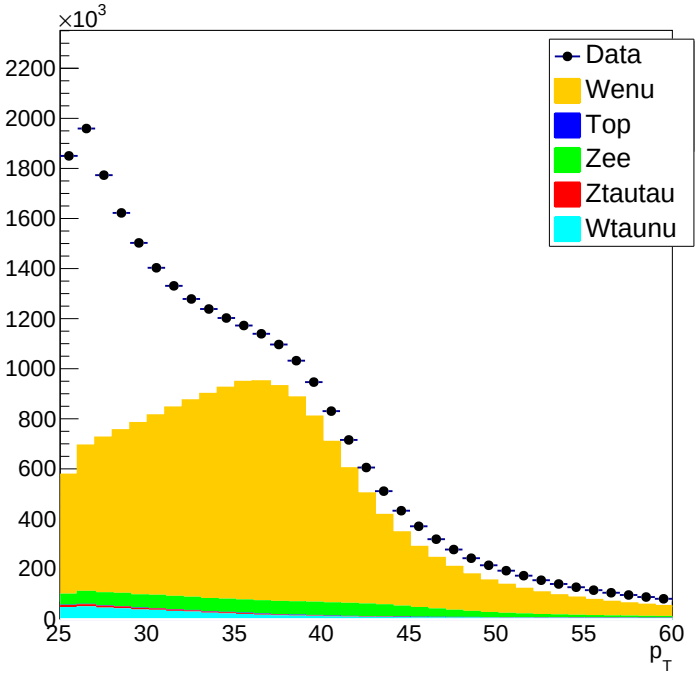

Figure 3.23: Transverse momentum p_T of data, simulated data and background before applying further selection criteria.

Next, certain variables are plotted and the measured data is compared with the simulated data and background to define stricter selections based on these comparisons. The electron isolation *eliso* can be seen in Figure 3.24 (a). It is to be noted that for these and all further histogram another selection criterion has been chosen that fixes the number of electrons to exactly one.

In Figure 3.24 (b) the missing transverse energy $E_{T,\text{Miss}}$ is depicted, where all previous cuts including the additional cut on the electron isolation value $eliso < 0.3$ have already been applied to the data. By comparing the measured data with the simulation and background, decisions have to be made, that properly reduce e.g. the green $Z \to e^- e^+$ background while still keeping as much significant $W \to e\nu$ data as possible. Thus, a cut at $E_{T,\text{Miss}} > 25\,\text{GeV}$ has been chosen next.

Another important criterion is the transverse mass m_T, which was calculated with the implemented function `mT()` and which can be seen in Figure 3.24 (c). From this, a transverse mass of $m_T > 40\,\text{GeV}$ has been chosen. Applying all of these cuts to the p_T histogram, yields figure 3.24 (d). Other possible cut parameters have been studied accordingly but did not yield any significant result or were continuous throughout their parameter range.

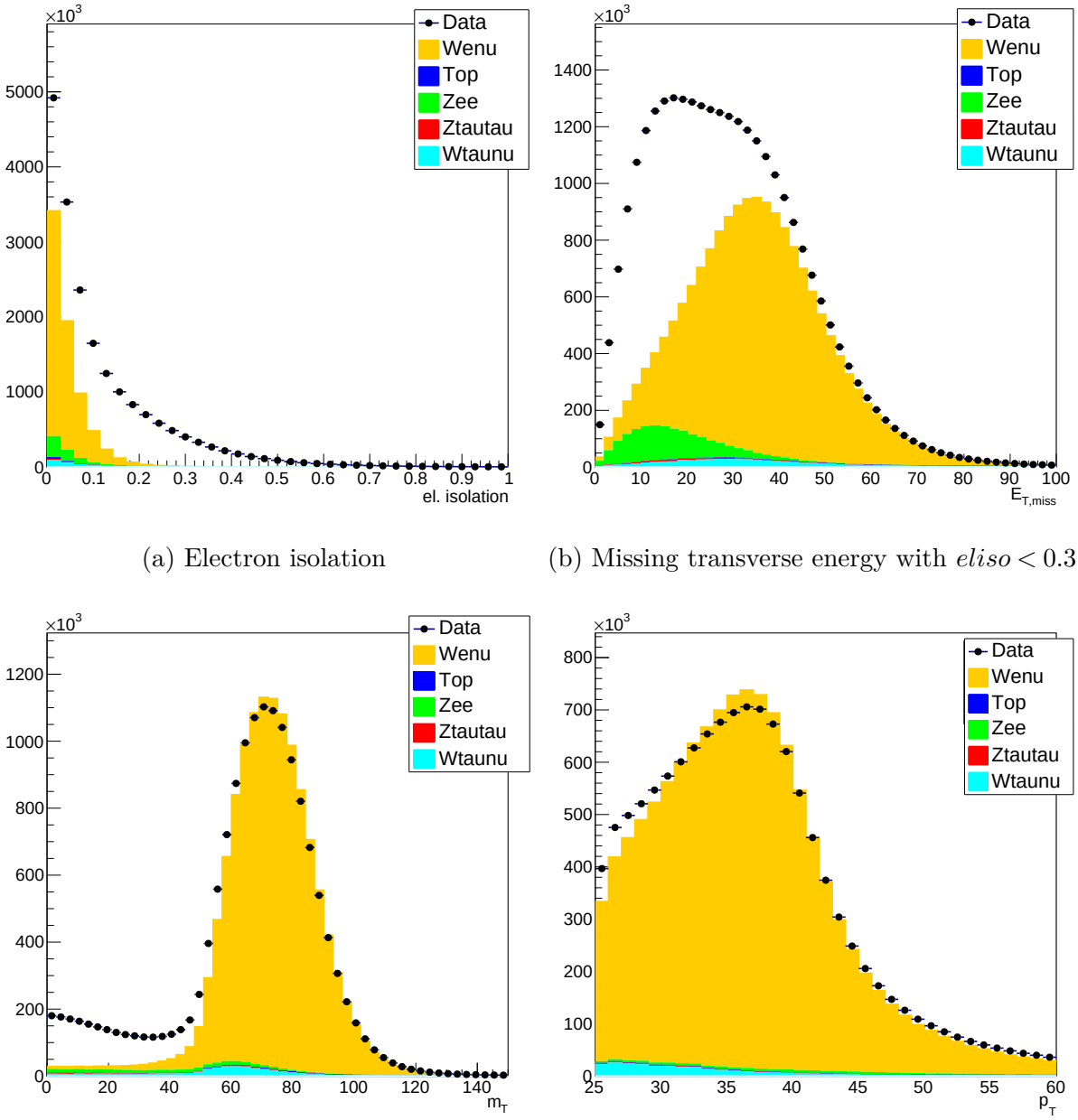

(a) Electron isolation

(b) Missing transverse energy with $eliso < 0.3$

(c) m_T with $eliso < 0.3$ and $E_{T,\text{miss}} > 25\,\text{GeV}$

(d) p_T with all cuts including $m_T > 40\,\text{GeV}$

Figure 3.24: Selection criteria and p_T with selections applied for $m_W = 80\,\text{GeV}$

Obviously the data fits the expectation much better, although there are still some discrepancies. These can be improved via adding QCD background and finding the ideal W mass so the data can be weighted accordingly. The QCD background stems from QCD jets, which can be misinterpreted as electrons. Thus, the criteria for these events are the identification as one electron, but an electron isolation value opposite from the above selection (so $eliso > 0.3$).

3.3.3 Determination of m_W

In order to find the correct QCD background scaling factor and W mass, a two-dimensional loop was used for finding the ideal value for both quantities, which minimises the χ^2 value between data and background processes. The loop goes through masses ranging from 79.6 GeV

to 80.5 GeV and QCD values between 0 and 4.5. This range of QCD values was chosen due to a previous scan of a larger parameter range. Then the the following polynomial

$$f(x,y) = p0 + p1(x-p2)^2 + p3(y-p4)^2 \tag{3.3}$$

is fitted to a two-dimensional histogram which can be seen in Figure 3.25. The parameters of interest are $p2$, which represents the minimum's position on the mass axis, and $p4$ standing for the QCD scale factor belonging to the minimum.

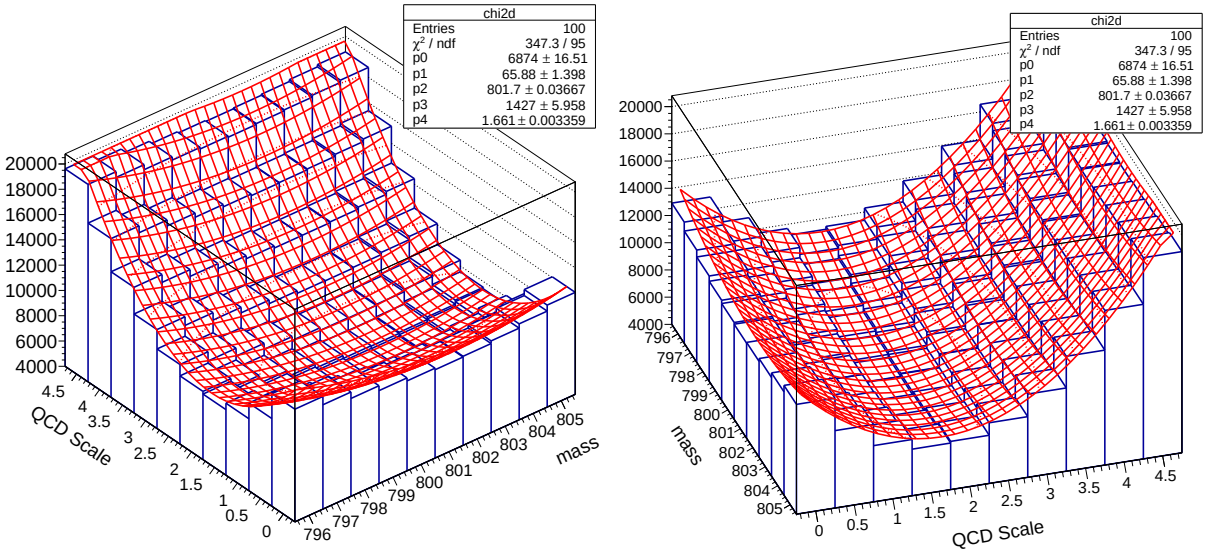

Figure 3.25: Histogram for QCD scaling and m_W that minimise the χ^2 value between simulated and measured data.

The χ^2 value was calculated using the bin contents and their respective errors for both simulated values and real data:

$$\chi^2 = \frac{(x_{\text{sim}} - x_{\text{data}})^2}{\sigma_{\text{sim}}^2 + \sigma_{\text{data}}^2} \tag{3.4}$$

This fit yields a preferred QCD scaling value of ≈ 1.7 and a W mass of

$$m_W = (80.2 \pm 0.1)\,\text{GeV}.$$

The uncertainty was estimated by considering the bin size of the histogram. Since the bins have a certain width, it is only known, that the fit result lies somewhere within the bin. The possible range is thereby confined by the neighbouring bins. The error on $p2$ originating from the fit is is omitted here, due to the larger statistic uncertainties.

All of the additionally applied cuts and criteria are summarised in Table 3.3.

Parameter	value
number of e	1
el. isolation	< 0.3
$E_{T,\text{Miss}}$	$> 25\,\text{GeV}$
m_T	$> 40\,\text{GeV}$
QCD scaling	1.7
m_W	80.2 GeV

Table 3.3: Summary of the cut variables used to determine the W mass.

The previous p_T plot now weighted according to the determined mass and QCD scaling factor can be seen in Figure 3.26. It is evident, that the simulation fits the data much better now.

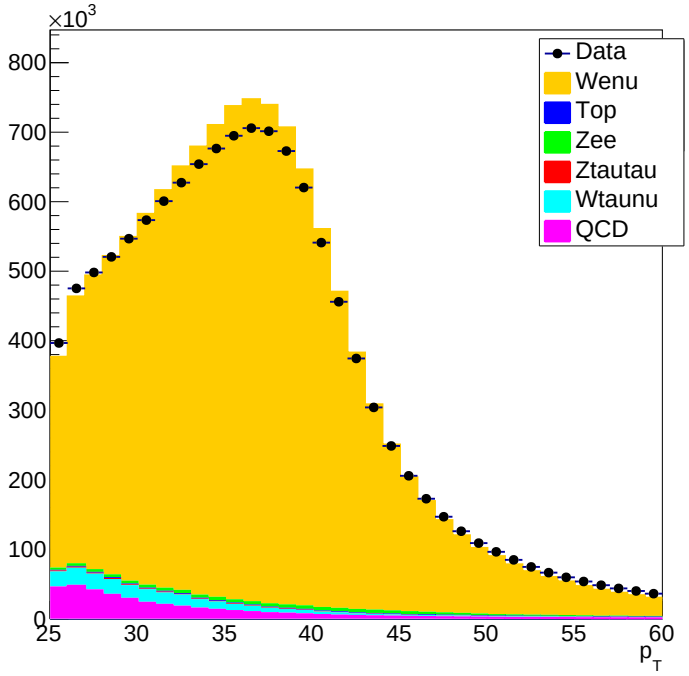

Figure 3.26: Transverse momentum p_T of data, simulated data and background with all chosen selection cuts and QCD scaling for $m_W = 80.2\,\text{GeV}$.

Although an uncertainty for m_W was estimated, this error does not include all possible statistical and systematic errors, which could occur in the chosen procedure of determining the W mass. To go into more depth, calibration errors from the calibration performed in Section 3.2 would need to be taken into account and propagated to the end result. Using the two-dimensional calibration instead of the one-dimensional would probably lead to an even better result. Additionally, weighting using the `getWeights()`function is also subject to systematic errors, since it does not use simulated data for all the different masses, but the Breit-Wigner fit is only shifted according to these.

3.4 Search for the Higgs boson

A goal of great interest at the ATLAS detector is the discovery of new physics and particularly new particles. The events indicating processes, that have not been observed before, are assumed to happen much more rarely. This means, that careful statistical evaluation of measured processes is crucial, which is why this experiment gives a short introduction to this topic. The main goal of the last task is to find the Higgs boson. Therefor, the decay of the Higgs boson in four leptons $H \to ZZ \to 4l$ is used. Here, the leptons are restricted to electrons or muons. However, extracting the Higgs decay is no easy task due to the background processes which can display a similar signature as the sought-after process and happen much more frequently. These background processes are namely

$$\begin{aligned} Z &\to ll\, b\bar{b} \\ t\bar{t} &\to ll\, b\bar{b}\, \nu\overline{\nu} \\ WZ &\to l\nu\, l'l' \\ Z &\to ll \\ ZZ &\to 4l \end{aligned}$$

whereby the the Z-bosons from the last decay arise from ZZ pair production. This process is the only one within the standard model to show the same signature as the Higgs decay regarded in this part. It is vital to carefully filter out these background events in order to observe the decay of interest as pure as possible. This is done by cutting at certain variables which allow to lose background signals while at the same time keeping as much of the Higgs signal as possible.

In order to extract the Higgs decay from all data, Monte Carlo simulations for all possible background processes and the various Higgs production mechanisms are considered. These simulations are used to examine the various kinematic variables and parameters. They are helping to find the variables then used for separating the signal from the background processes. On these variables, cuts are chosen by regarding the $\frac{s}{\sqrt{b}}$ value. Afterwards, these cuts are then used on real data measured at the ATLAS detector. The significance and the p-value then state if the Higgs boson was discovered. This is all done with the provided C++ file `analysis.cpp`and will be explained in detail in this section.

3.4.1 Finding the optimal cuts on the different variables

To begin with, histograms of the different kinematic variables are regarded in order to select the candidates suitable for separating between Higgs and background events. The goal is then to extract the signal from the Higgs decay by cutting away as much as possible from the various background processes. The parameter of interest is the invariant mass M_{4l} of all four leptons, which corresponds to the mass of the Higgs boson. Figure 3.27 shows the M_{4l} histogram before any selections were used. It is obvious, that the Higgs signal is superimposed by the background events. This needs to be changed improved the following.

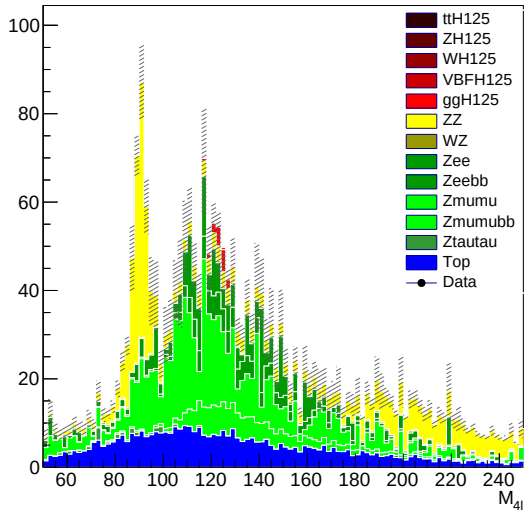

Figure 3.27: Invariant mass of all four leptons before applying any cuts. The upper five events in shades of black and red represent the signal events that are to be extracted while the other colours symbolise background processes.

For finding the optimal cuts, the ratio $\frac{s}{\sqrt{b}}$ is considered, where b is the expected number of background events based on theory and s is the number of signal events. This ratio is to be maximised in order to obtain a signal as pure as possible from the background events without loosing too much of the signal.

In the following, the histograms belonging to the respective variable will be shown together with the scanning histograms which contain the ratio $\frac{s}{\sqrt{b}}$, from which the cuts are derived. These scanning histograms can be obtained with the function `ScanHistograms()`already provided in the given code. In these plots, the signal is depicted in red, the background is represented by the blue histogram, which is filled with grey, and $\frac{s}{\sqrt{b}}$ is drawn as black crosses. These histograms are available for the lower and upper cut. For both cases, the optimal cut can be found by looking at the maximum of $\frac{s}{\sqrt{b}}$. Nevertheless, these cuts have to be examined carefully to avoid cutting away too much of the signal.

Transverse momentum

The first considered variable is the transverse momentum p_T of the four different leptons. Figure 3.28 displays p_T for lepton 1 together with the scanning histogram used for finding the appropriate lower cuts. Hereby, the first lepton corresponds to the lepton with the largest p_T while lepton 4 holds the lowest transverse momentum. The according histograms for the other three leptons can be found in the appendix in Figure 5.1, 5.2 and 5.3. With the help of these plots, the following lower cuts were chosen:

- lepton 1: $p_T \geq 26\,\text{GeV}$
- lepton 2 $p_T \geq 18\,\text{GeV}$
- lepton 3 $p_T \geq 13\,\text{GeV}$
- lepton 4: $p_T \geq 8\,\text{GeV}$

The decrease of the lower cut values matches the previously mentioned sorting according to the transverse momentum.

Considering the upper cut histograms, it was decided not to use a cut on the upper limits of the transverse momenta. There was no clear maximum identifiable. The according plot for p_T of lepton 1 as an example can be seen in Figure 3.29,

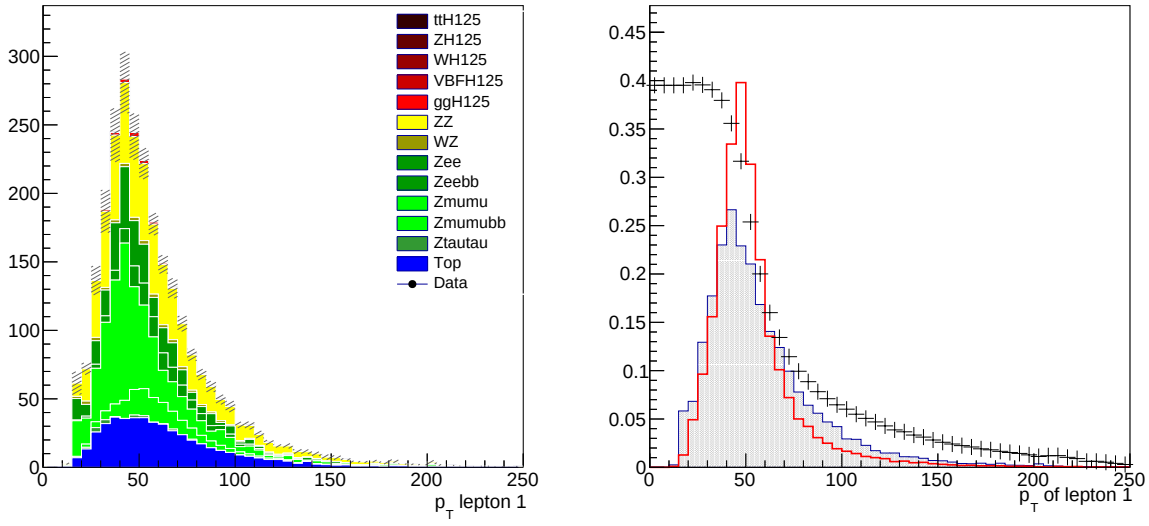

(a) transverse momentum of lepton 1 (b) upper cut of lepton 1

Figure 3.28: Histogram of the transverse momentum of lepton 1 together with its lower cut

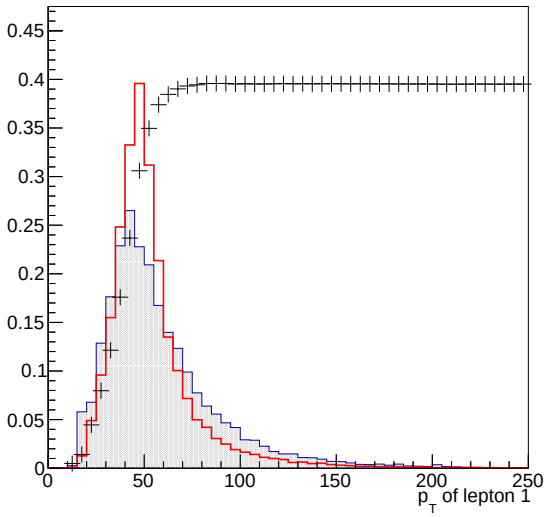

Figure 3.29: Upper cut on p_T of lepton 1

Number of leptons:
Since the goal is isolating the decay of Higgs in four leptons, the number of leptons is restricted to 4. As can be seen in Figure 3.30, there has also been a small amount background events with five leptons, which are to be to excluded. Any events with less than four leptons have already been excluded in `analysis.cpp` before, thus cutting on the lower limit is not necessary.

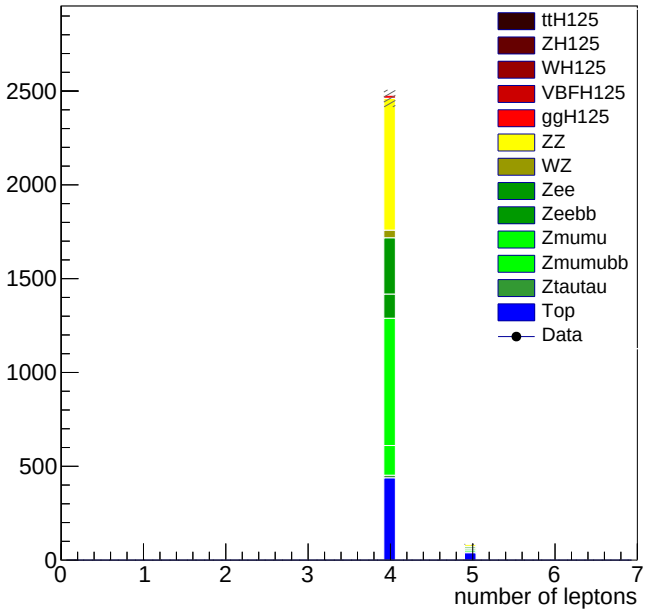

Figure 3.30: Histogram of the number of leptons

Calorimeter isolation:
The calorimeter isolation *etiso* helps to distinguish electrons from photons. It is defined as the ratio of the energy within the cone of the shower in the ECAL and the rest energy of an electron. Since electrons have a small shower compared to the photons arising among others from the pion decay $\pi^0 \to \gamma\gamma$, the idea is to determine an upper limit for the calorimeter isolation. This should exclude photons. The histogram of the isolation value for lepton 1 as an example can be found in Figure 3.31. It also includes the corresponding scan histograms with $\frac{s}{\sqrt{b}}$. The plots for the other leptons are depicted in Figure 5.4, 5.5 and 5.6 in the appendix. With this plot the decision is made on the following upper cuts:

- lepton 1 and 2: $etiso < 0.15$
- lepton 3 and 4: $etiso < 0.1$

Here, the first lepton does not necessarily correspond to the lepton with the highest transverse momentum p_T.

Figure 3.32 suggests, that a constraint of the lower range for the calorimeter isolation is not necessary.

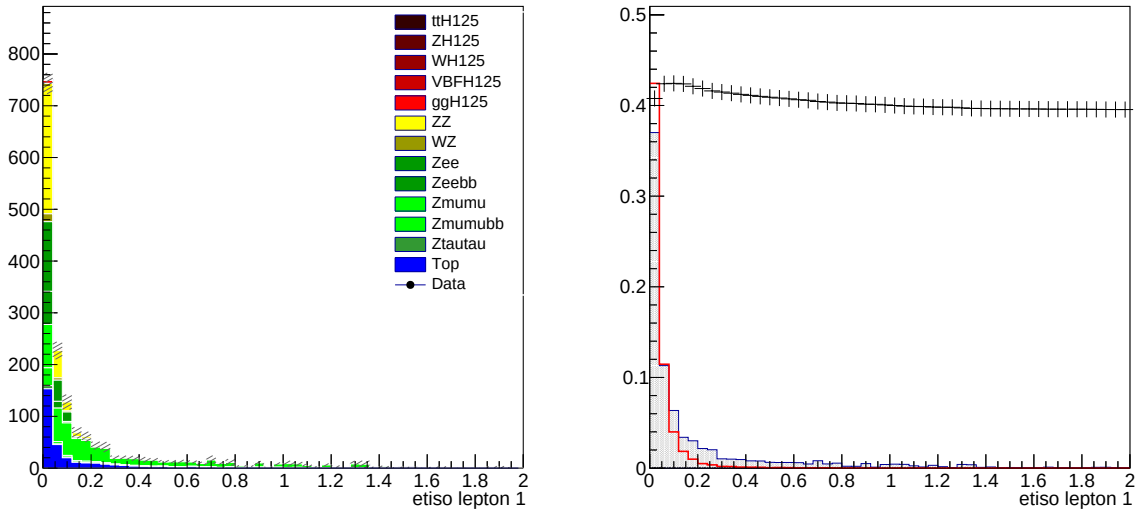

(a) calorimeter isolation of lepton 1 (b) upper cut of lepton 1

Figure 3.31: Histogram of the calorimeter isolation of lepton 1 together with the upper cut histogram

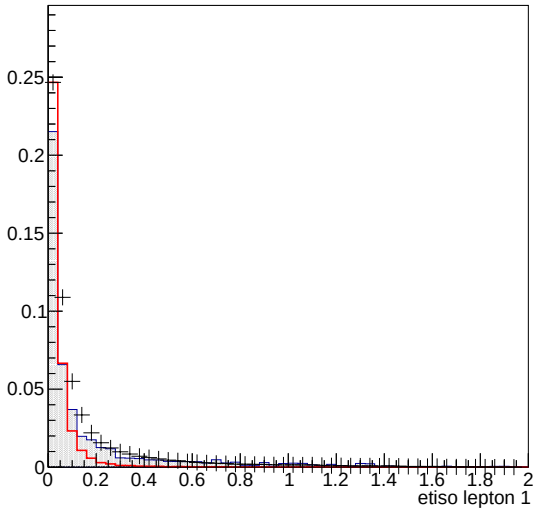

Figure 3.32: Lower cut on calorimeter isolation of lepton 1

Track isolation:
After considering the track isolation *ptiso*, the idea of using the track isolation as a selection criterion was discarded, since there exists neither for lower nor for the upper cut a real maximum of $\frac{s}{\sqrt{b}}$. The histogram belonging to lepton 1 can be seen in Figure 3.33 and the corresponding scanning histograms for the upper and lower cut for an exemplary lepton are depicted in Figure 3.34. Again, lepton 1 does not stand for the lepton with the highest p_T.

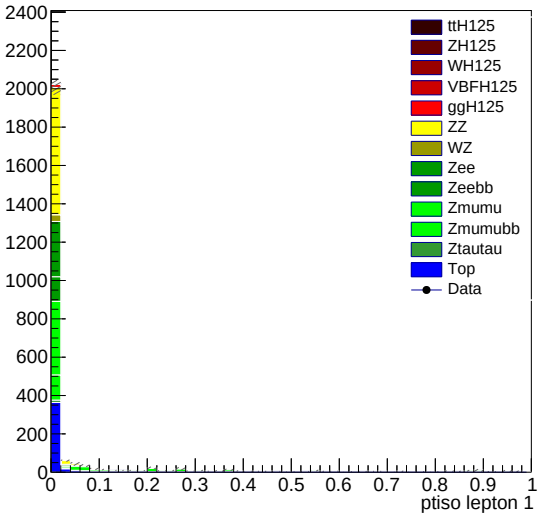

Figure 3.33: Histogram of the track isolation of lepton 1

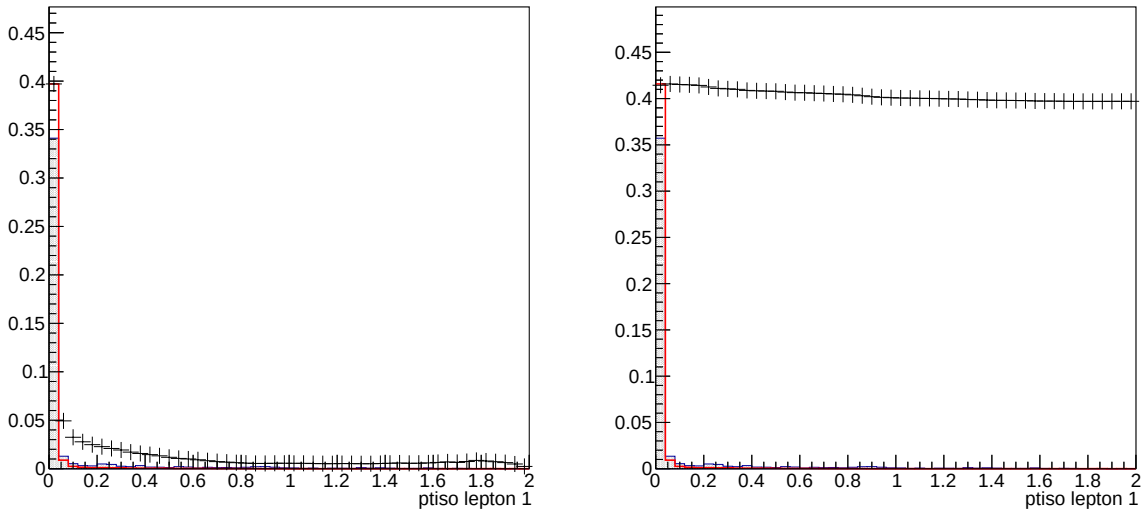

(a) lower cut of track isolation

(b) upper cut of track isolation

Figure 3.34: Scanning histogram for lower and upper cut of the track isolation for the first lepton.

Impact parameter significance $\frac{d_0}{\sigma_{d_0}}$:
The variable d_0 is the transverse impact parameter and σ_{d_0} names the corresponding error. The according histogram for $\frac{d_0}{\sigma_{d_0}}$ of lepton 1 can be seen in 3.35 together with the scanning histogram for the upper cut. The respective histograms for lepton 2-4 can be found in the appendix in Figure 5.7, 5.8, 5.9. After considering the lower cut scanning histogram, see Figure 3.36, no lower constraint was used. Thus, the choice fell on the following upper cuts:

- lepton 1 and 2: $\frac{d_0}{\sigma_{d_0}} < 2.5$
- lepton 3 and 4: $\frac{d_0}{\sigma_{d_0}} < 2$

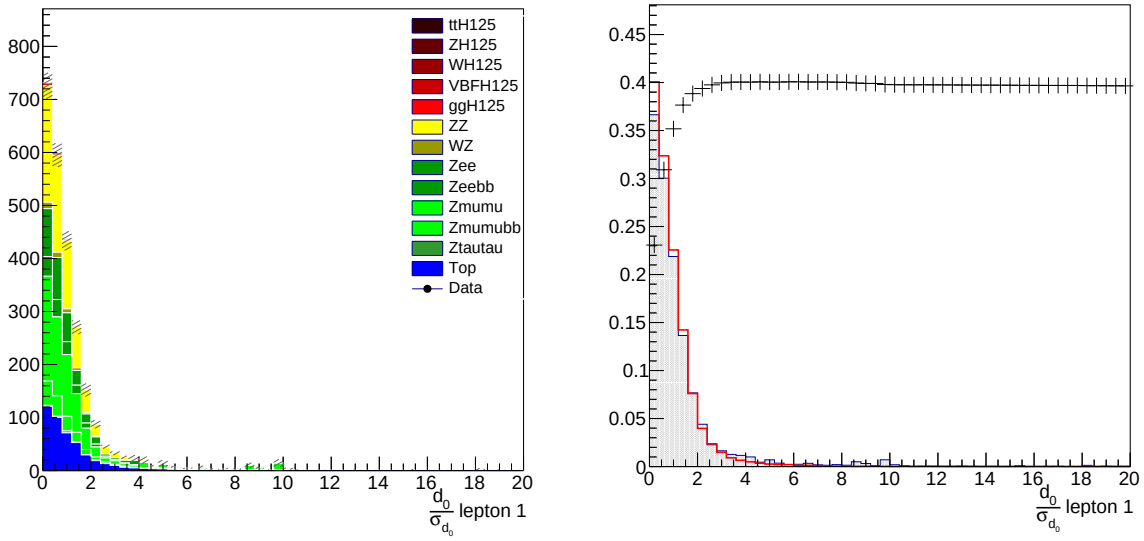

(a) impact parameter significance of lepton 1 (b) upper cut of lepton 1

Figure 3.35: Histogram of the impact parameter significance with the upper cut histogram for lepton 1

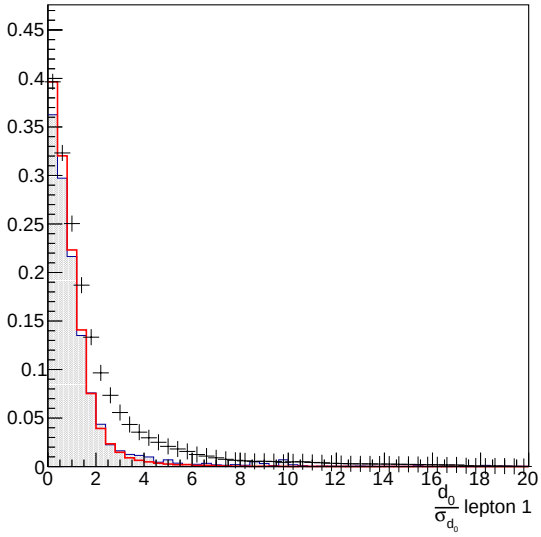

Figure 3.36: Scanning histogram for the lower cut of $\frac{d_0}{\sigma_{d_0}}$ of lepton 1

Impact parameter significance $\frac{z_0}{\sigma_{z_0}}$:
Because the transverse impact parameter is already used as a cut variable and the scanning histograms did not suggest a sensible cut, the ratio of the longitudinal impact parameter z_0 and its error σ_{z_0} is not chosen as a selection criterion. The corresponding histogram can be seen in Figure 3.37.

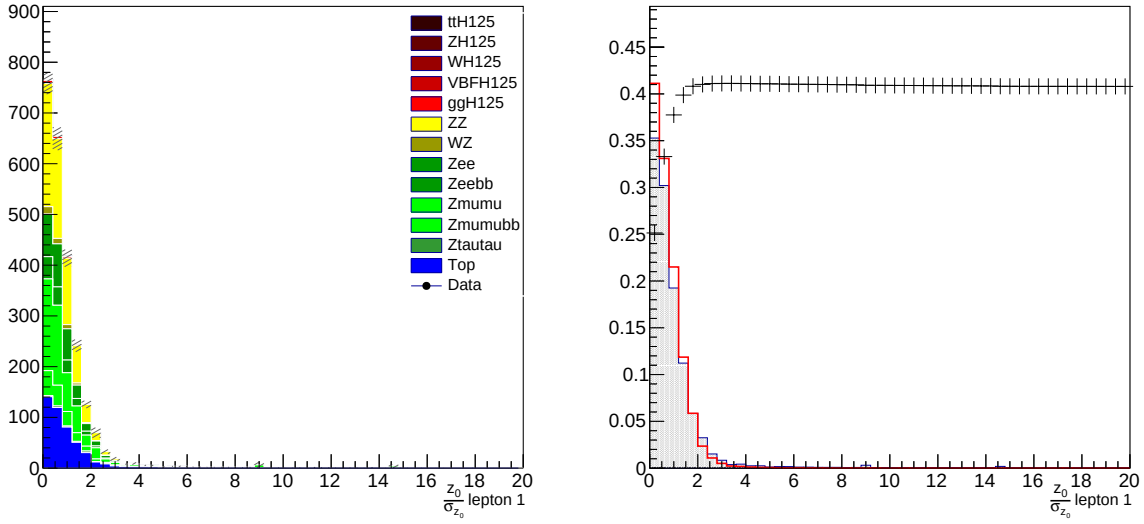

(a) $\frac{z_0}{\sigma_{z_0}}$ of lepton 1 (b) scanning of $\frac{z_0}{\sigma_{z_0}}$ of lepton 1

Figure 3.37: Impact parameter significance $\frac{z_0}{\sigma_{z_0}}$ of lepton 1 and scanning histogram

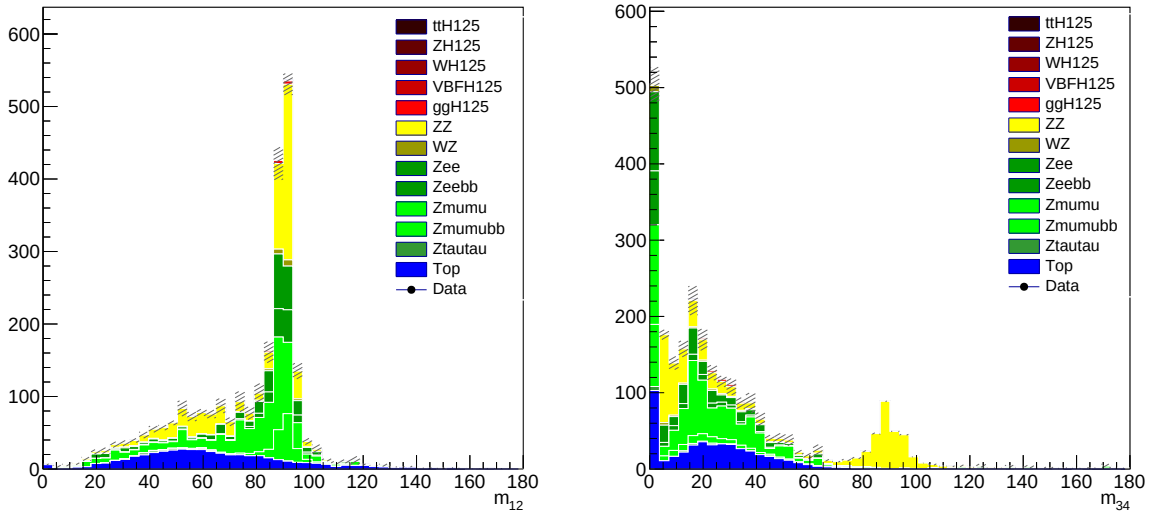

(a) invariant mass m_{12} (b) invariant mass m_{34}

Figure 3.38: Histogram of the invariant masses m_{12} and m_{34}.

Invariant masses:
Next, the invariant masses m_{12} and m_{34} are considered, which can be seen in Figure 3.38. The former is the invariant mass of the two leptons which yield a result closest to the mass of a Z boson. m_{34} then combines the remaining two leptons. These masses are two of the most important cut criteria since they can be used to differ between the $H \to ZZ \to 4l$ decay and the decay of the two via ZZ-pair production created Z bosons $ZZ \to 4l$. While the two Z bosons of the second decay are both real, the Higgs decay includes one real and one virtual Z boson. Thus for $ZZ \to 4l$, m_{12} and m_{34} are both approximately located at the mass of a Z boson,

while for the Higgs decay this can only be said about m_{12}. m_{34} can then be found at a smaller mass range. This statement is supported by the scanning histograms including $\frac{s}{\sqrt{b}}$, which can be found in Figure 3.39. Altogether, the choice was made to use the following cuts:

- m_{12}: $62\,\text{GeV} < m_{12} < 97\,\text{GeV}$
- m_{34}: $8\,\text{GeV} < m_{34} < 57\,\text{GeV}$

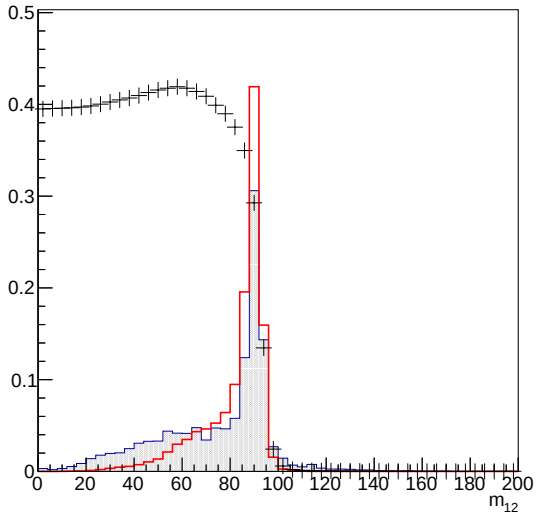

(a) lower cut on m_{12}

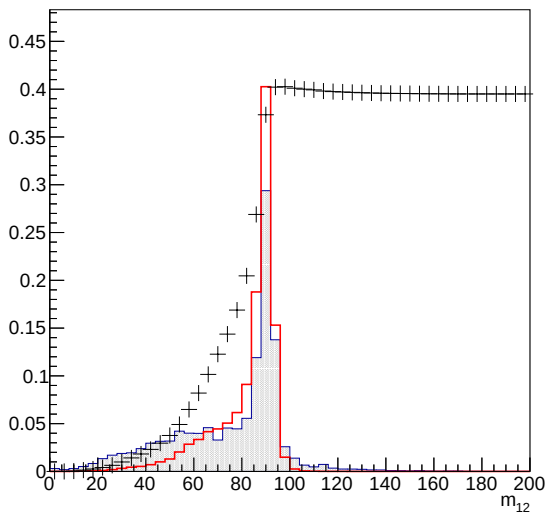

(b) upper cut on m_{12}

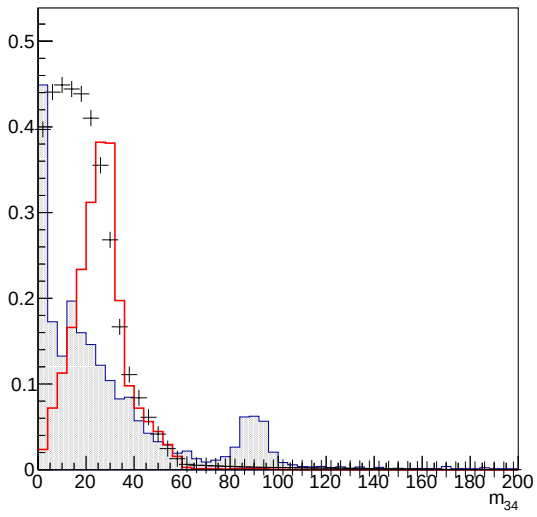

(c) lower cut on m_{34}

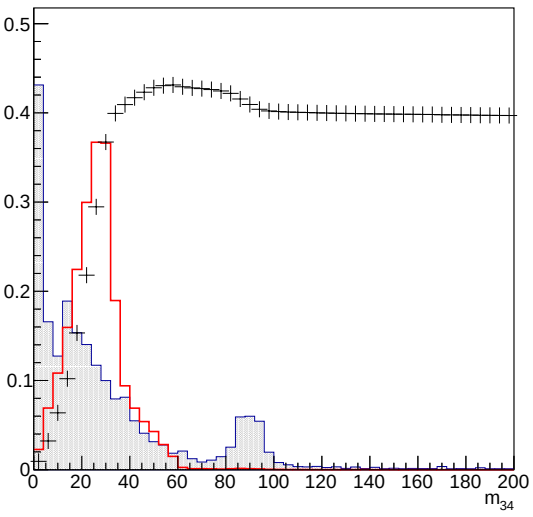

(d) upper cut on m_{34}

Figure 3.39: Scanning histogram of the invariant masses. Figure (a) and (b) contain the cuts on m_{12} and figure (c) and (d) depict the cuts on m_{34}.

Missing Transverse Energy:
The histogram of the missing transverse energy MET can be found in Figure 3.40. An assumption standing to reason would be, that an upper cut would help at extracting the signal

from the background, since no neutrinos are involved in the sought-after Higgs decay. Yet, the according scanning histogram does not support the usefulness of a cut on MET, see Figure 3.41. There is no distinct maximum recognisable.

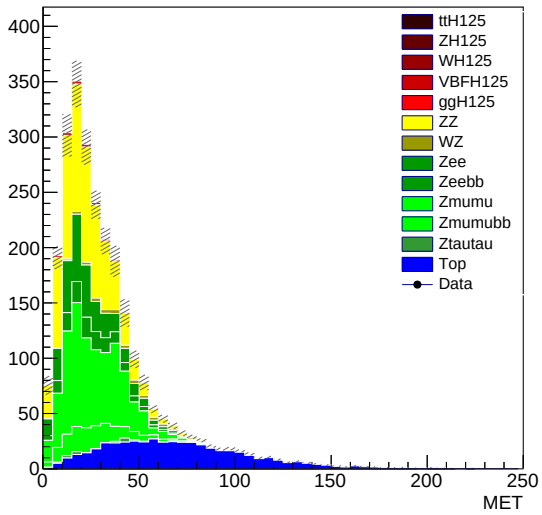

Figure 3.40: Histogram of MET

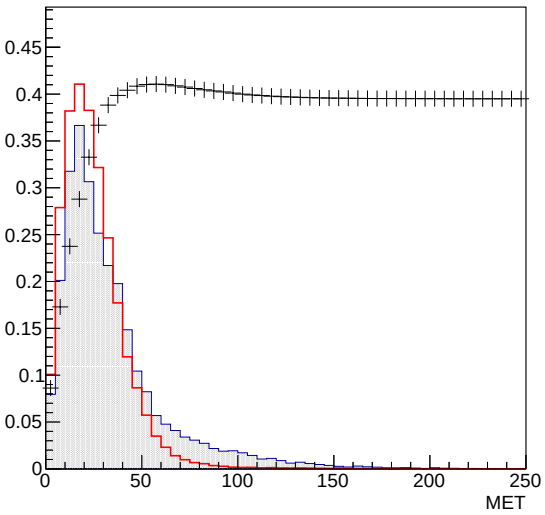

Figure 3.41: Upper cut on MET

Coordinates ϕ and η:
The histograms of ϕ and η, which represent the coordinates in the coordinate system used at ATLAS, can be found in Figure 3.42. Yet, in the respective histograms there is no difference between the distribution of the signal and the background events. Hence, it does not make sense to cut on these coordinates.

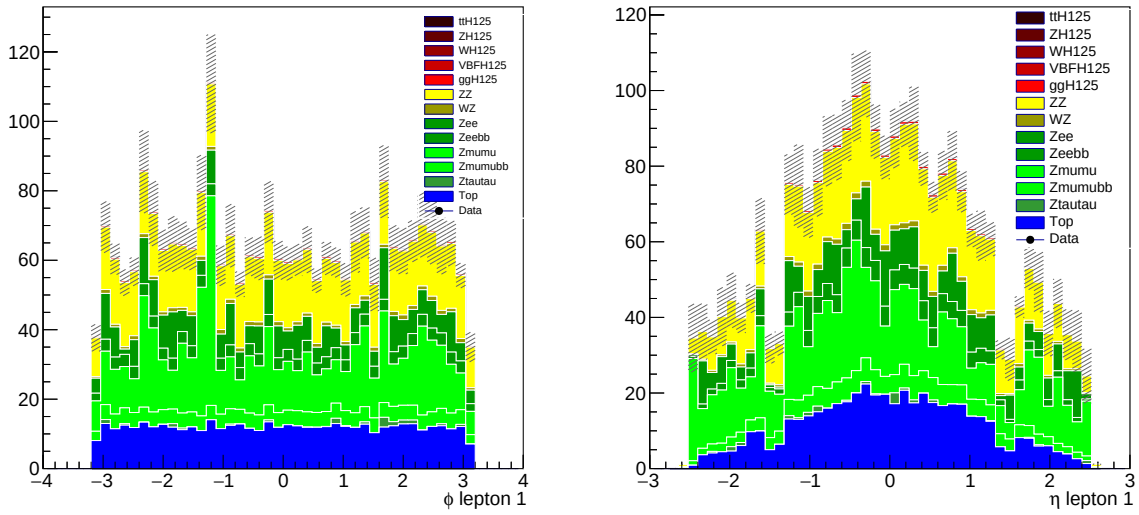

(a) azimuthal angle ϕ

(b) pseudorapidity η

Figure 3.42: Histograms of the azimuthal angle ϕ and the pseudorapidity η.

In order to give an overview, a composition of all chosen cuts can be found in Table 3.4.

Parameter	cut type	value
p_T lepton 1	lower	$\geq 26\,\text{GeV}$
p_T lepton 2	lower	$\geq 18\,\text{GeV}$
p_T lepton 3	lower	$\geq 13\,\text{GeV}$
p_T lepton 4	lower	$\geq 8\,\text{GeV}$
number of leptons	upper	$= 4$
etiso lepton 1 & 2	upper	< 0.15
etiso lepton 3 & 3	upper	< 0.10
$\frac{d_0}{\sigma_{d_0}}$ lepton 1 & 2	upper	< 2.0
$\frac{d_0}{\sigma_{d_0}}$ lepton 3 & 4	upper	< 2.5
m_{12}	lower	$> 62\,\text{GeV}$
	upper	$< 97\,\text{GeV}$
m_{34}	lower	$> 8\,\text{GeV}$
	upper	$< 57\,\text{GeV}$

Table 3.4: Summary of the variables on which cut conditions were applied together with the corresponding cut values

3.4.2 Invariant mass m_{4l} after applying the cuts

After applying all the cuts mentioned in the section before, the invariant mass is plotted again. This plot then shows if the extraction of the signal events from the background was successful. For direct comparison, Figure 3.43 contains the invariant mass histogram before and after the cuts.

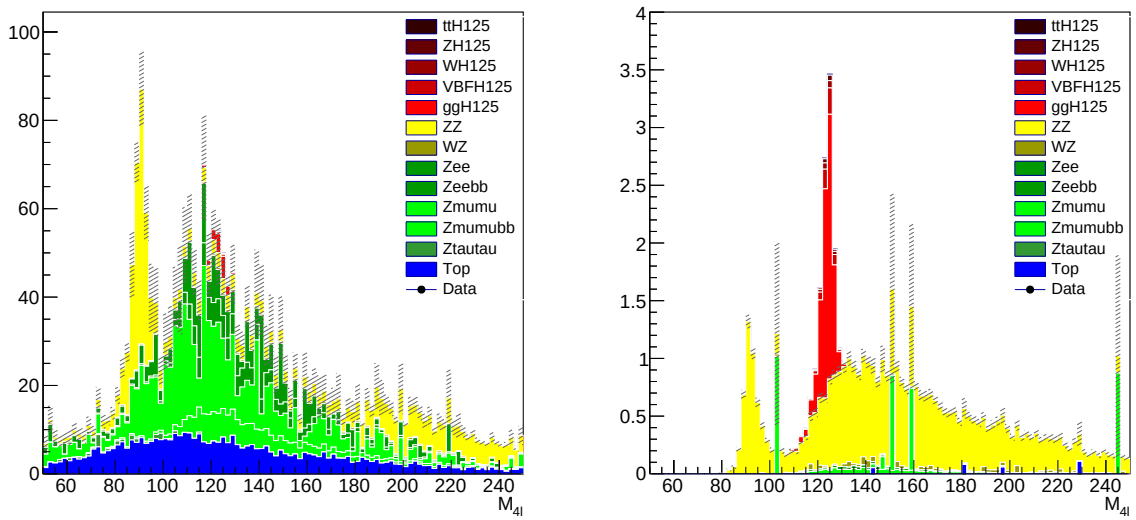

(a) before cuts

(b) after cuts

Figure 3.43: Histograms of the invariant mass M_{4l} before and after applying any cuts.

It seems like the event signals were successfully filtered out from the background processes. In the next part, this extracted data set is compared to real ATLAS data. Figure 3.44 shows the new event selection together with the selected data.

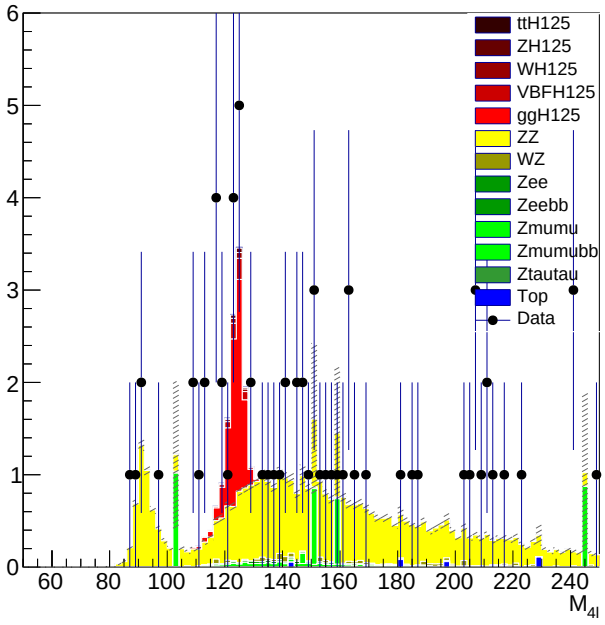

Figure 3.44: Histogram of the invariant mass with applied cuts together with real ATLAS data.

3.4.3 Statistical Evaluation

In a next step, the p-value is observed together with the significance for the real data and the simulation data with the applied selections. The null-hypothesis is the background-only hypothesis, which means, that the number of signal events $s = 0$ and the number of background events b corresponds to the number of counted events n. The expected number of events is the number of background events b, due to the chosen hypothesis. The p-value p_0 is the probability of obtaining a result, which is equal or less compatible than the observed number of events, compare Figure 3.45. Here, observed stands for the measured data. The significance Z can be expressed through the p-value by

$$Z = \Phi^{-1}(1 - p_0), \tag{3.5}$$

with Φ as a cumulative Standard Gaussian with mean value 1 and variance 0.

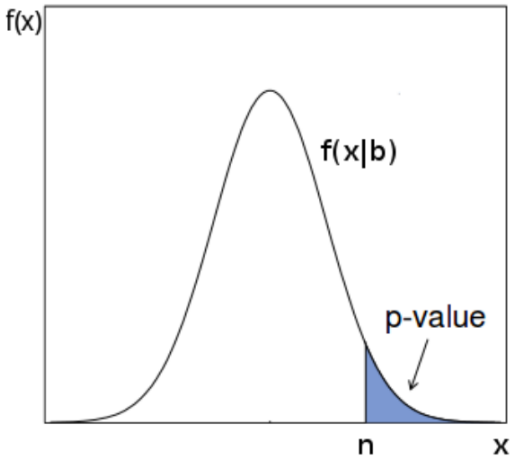

Figure 3.45: Graphical representation of the p-value as the probability of obtaining a result, that fits or is even less compatible than the expected result [3].

In order to state, that a particle was observed, a significance of at least $Z = 5$ is obligatory. Only then the probability that the particle is only a statistical fluctuation, is sufficiently small. However, this hypothesis has to be tested. Therefor, an *Asimov* data set is used, which does not have real measured data as the observed events, but the simulated data for signal and background $(s + b)$. This sum of MC simulated events is called *pseudo data*. Nonetheless, the expected number of events is still the same as before for the real observed data, namely the number of background events b. With the Asimov data set, the *expected significance* is obtained while using the real data instead of the pseudo data as the observed events yields the *observed significance*. In this case, the expected significance is calculated with the function `PValue()` for different masses, each time within a window of 10 GeV, which is then shifted. Altogether, a range from $105\,\text{GeV} - 175\,\text{GeV}$ is covered with a step width of 10 GeV.

In the following, both the expected and the observed value are computed for the corresponding mass window and compared directly. Moreover, the respective significance shows, if the discovery of a Higgs boson has been made.

Figure 3.46 contains the observed p-value for the real data as observed events, while Figure 3.47 shows the p-value belonging to the expected significance using the Asimov data set as observed events. One can see that both plots have minima at approximately $m_H = 117\,\text{GeV}$ and $m_H = 144\,\text{GeV}$. Yet, the depths of these minima vary.
For the observed significance, a result of

$$Z = 3.12 \quad \text{for} \quad m = 115\,\text{GeV}$$

was obtained. While the largest expected significance obtained was:

$$Z = 3.00 \quad \text{for} \quad m = 145\,\text{GeV}.$$

The second maximum of the expected significance can be found between the 115 GeV and the 125 GeV mass window. Since the significance is related to the p-value via equation (3.5), the position of the largest significance corresponds to the position of the minimum of p_0. Thus, the mass value of the second largest observed significance matches the second minimum of the expected p-value and the other way round.

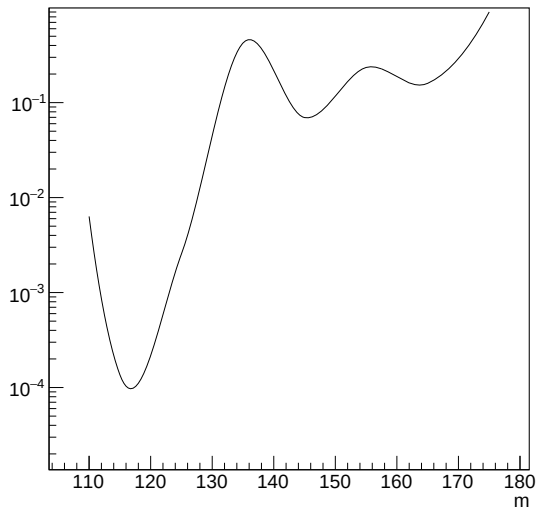

Figure 3.46: Observed significance

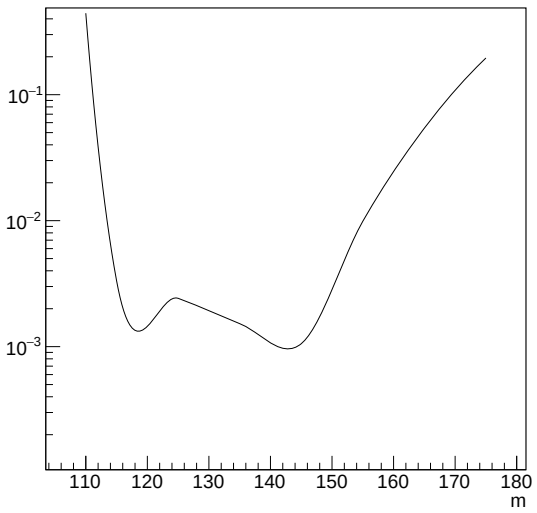

Figure 3.47: Expected significance

However, a significance of approximately $Z = 3$ is not enough to claim a discovery. Moreover, it is known that the mass corresponding to the smallest p-value should actually be $m_H = 125\,\text{GeV}$. As a consequence, an alteration of the cuts on the calorimeter isolation is tried because the former selections might have cut away too much signal. Before, the cuts had been $etiso < 0.15$ for lepton 1 and 2 and $etiso < 0.1$ for lepton 3 and 4. These were changed to

- lepton 1 and 2: $etiso < 0.18$
- lepton 3 and 4: $etiso < 0.08$.

These changes yield the following plots for the observed and expected significance, see Figure 3.48 and 3.49. It can be observed, that the position of the minimum for the observed significance has now shifted from $m_H \approx 117\,\text{GeV}$ towards $m_H \approx 125\,\text{GeV}$. Even if the expected p-value's minimum, which can now be found at $m_H \approx 120\,\text{GeV}$, does not coincide precisely with the minimum from the observed p-value, they lie within the same 10 GeV mass window.
The largest observed significance is now

$$Z = 2.92 \quad \text{for} \quad m = 125\,\text{GeV}$$

while the largest expected significance is

$$Z = 3.02 \quad \text{for} \quad m = 145\,\text{GeV}.$$

However, with a maximum of $Z = 3.00$ the significance is still not large enough to confirm the discovery of a Higgs boson.

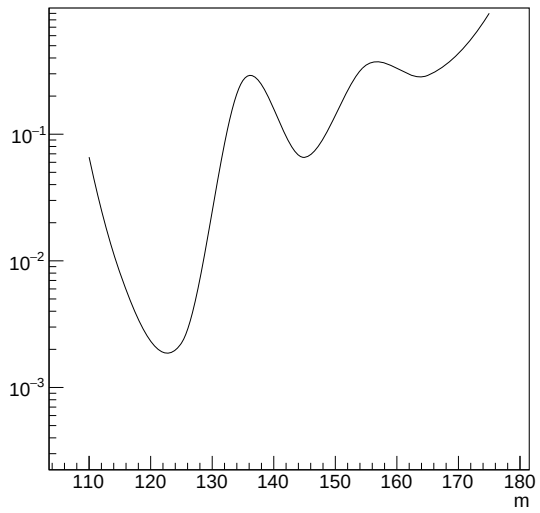

Figure 3.48: Observed significance (new *etiso*)

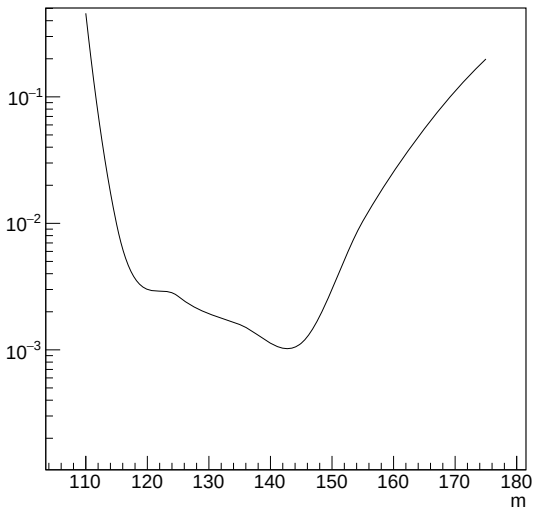

Figure 3.49: Expected significance (new *etiso*)

3.4.4 Signal strength

With the altered cut conditions used for the latest significance calculations, the signal strength is to be examined next. This is done by the provided function `FractionFit` within a certain range, which needs to be defined. The range used here together with the fit results can be found in Table 3.5.

fit range [GeV]	signal	background	signal SF	background SF
50-170	0.18 ± 0.13	0.82 ± 0.21	1.22	1.26

Table 3.5: Tabular containing the parameters from the signal strength fit. It contains the used fit range, the strength of both signal and background together with the scaling factors (SF) that the signal and background would have to be multiplied with, in order to match the data.

A scaling factor of 1 for both the signal and the background would mean, that the simulated data matches the measured data perfectly. However, the scaling is not yet perfect. If there would have been more time for this experiment, one could have determined the scaling factor of the background by chosing a certain control region, e.g. for the ZZ-pair production background process. There, one would mostly find ZZ background events and the measured data which allows the calculation of the scaling factor.

4 Summary and Conclusion

4.1 Graphical Evaluation of Particle Interaction with ATLANTIS

In the first part of this report, different event displays were regarded using the ATLAS event display ATLANTIS. Thereby, six different events were examined and assumptions for their respective decay processes were made. In each case either the invariant mass of all particles or the transverse mass, if neutrinos were involved, was calculated. The respective result was then used to check if the stated assumption is correct. The identified decay processes are:

$$
\begin{aligned}
Z &\to \mu^+\mu^- \\
W &\to \mu + \mu_\nu \\
t\bar{t} &\to \mu^+\mu^-\, b\,\bar{b}\,\nu_\mu\,\overline{\nu}_\mu \\
t\bar{t} &\to e^+e^-\, b\,\bar{b}\,\nu_e\,\overline{\nu}_e \\
H &\to ZZ \to \mu^+\mu^-\mu^+\mu^- \\
H &\to ZZ \to e^+e^-\mu^+\mu^-.
\end{aligned}
$$

The last two events are possible candidates for the decay channel that will later on be used for the search of the higgs boson. Thus, this decay process is crucial for this report.

4.2 Calibration of the electromagnetic Calorimeter

Before any calculations with measured data could be done, the electromagnetic calorimeter had to be calibrated. This was necessary because the electrons detected in the ECAL had already lost some of their energy while traversing the inner detector. The calibration was performed using the parametrisation

$$E_{meas} = E_{true}(1+\alpha)$$

where α had to be determined in this part of the experiment.
Therefor, the decay $Z \to ee$ was used together with the fact that the Z boson mass is known. The calibration was performed by fitting a Breit-Wigner-function to the invariant mass of the electrons and calculating α. Without any calibration, the invariant mass yielded

$$M_{ee} = 83.9\,\mathrm{GeV}$$

The selections used for calibrating were then chosen by how close the according calibration comes to the known Z mass. Thereby, both a one-dimensional calibration in the pseudorapidity η and a two-dimensional calibration in η and the transverse momentum p_T was implemented. Both lead to the same result of

$$M_{ee} = 90.5\,\mathrm{GeV}$$

for the invariant mass of the two electrons. This value is close to the standard model Z mass of $M_Z = 91.2\,\mathrm{GeV}$ (see Figure 2.1). Since the results for the 1d- and 2d-calibration lead to the same result and since only the one-week experiment was performed, the one-dimensional calibration was used in the next part.

4.3 Measurement of the W mass

With usage of the one-dimensional calibration performed in the previous part, the mass of the W boson was determined using the $W \to e\nu$ decay. Through weighting simulated data and

background data and comparing different kinematic variables with those of the measured data, suitable cut criteria could be found to minimise background and misidentification probability. These cuts have been applied to the measured data and for further background elimination a properly scaled QCD background was added. The background was scaled to the data according to a two-dimensional loop finding the best value for the QCD scaling and W mass m_W by minimising the χ^2 value between simulated and measured data. Using a two-dimensional fit to find these values yielded a mass of

$$m_W = (80.2 \pm 0.1)\,\text{GeV}$$

whereas the literature value is $m_W = (80.385 \pm 0.015)\text{GeV}$ [3]. The determined W mass matches the literature value within two standard deviations and thus seems like a good estimate. However, it should be noted that due to time restrictions a proper error determination including systematic errors has not been performed. Additionally the method of obtaining m_W could be improved by using the two-dimensional calibration of the electromagnetic calorimeter instead of the one-dimensional.

4.4 Search for the Higgs boson

In the last task, the search for the Higgs boson at the ATLAS detector was reproduced. The decay channel which was examined is the Higgs decay into 4 leptons $H \to ZZ \to 4l$. Therefor, Monte Carlo sampled data of the Higgs decay with Higgs mass of $m_H = 125\,\text{GeV}$ was considered together with simulated events of several important background processes. With this created data, the different kinematic variables of the processes were considered. By looking at the ratio $\frac{s}{\sqrt{b}}$, different lower and upper cuts were determined aiming at extracting the signal from the background events. After these cuts were applied, the real data was added together with MC simulations of Higgs events for different Higgs-masses in a range from $(110 - 175)\text{GeV}$. They were used to create an Asimov data set and both the observed and the expected p-value and the corresponding significances were calculated. However, the significances obtained by this method with a maximum of $Z = 3.12$ are too small to state the discovery of the Higgs boson.

5 Appendix

Search for the Higgs boson

Transverse momentum

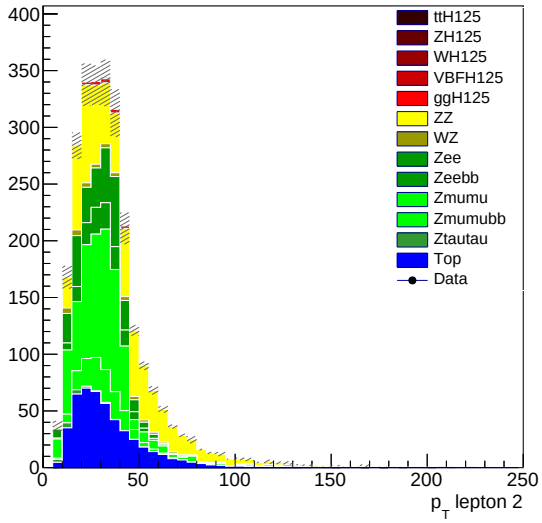

(a) transverse momentum of lepton 2

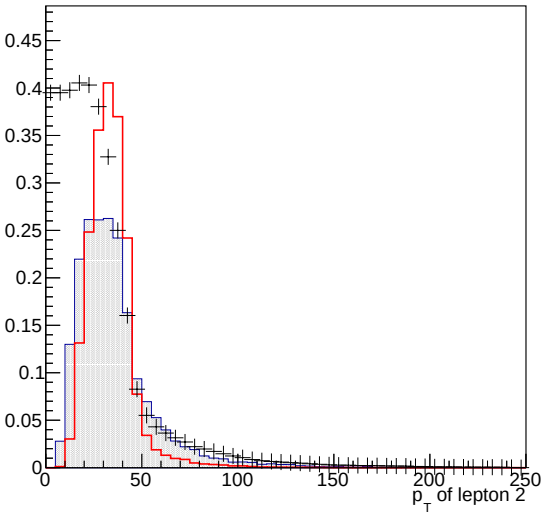

(b) upper cut of lepton 2

Figure 5.1: Histogram of the transverse momentum of lepton 2 together with its lower cut

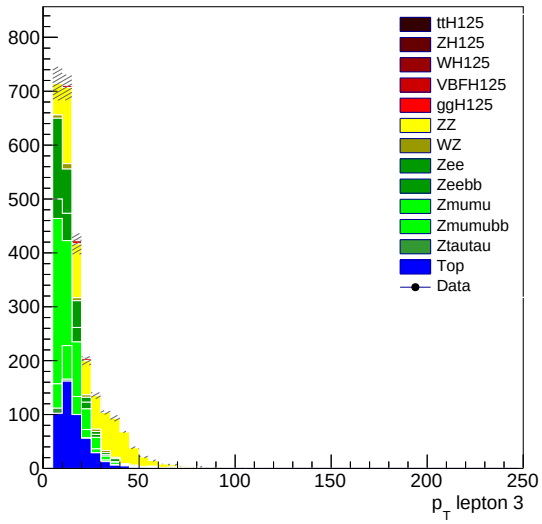

(a) transverse momentum of lepton 3

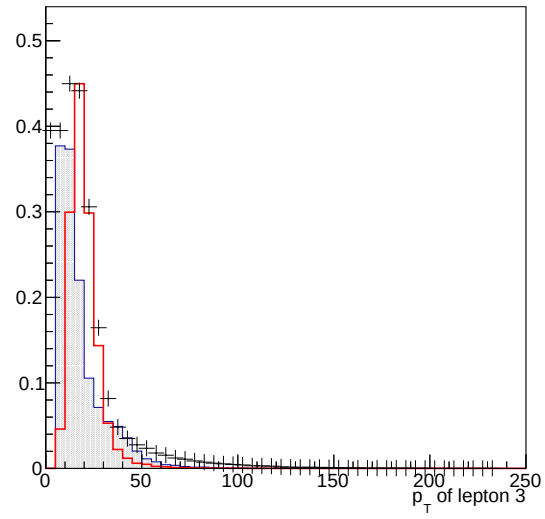

(b) upper cut of lepton 1

Figure 5.2: Histogram of the transverse momentum of lepton 3 together with its lower cut

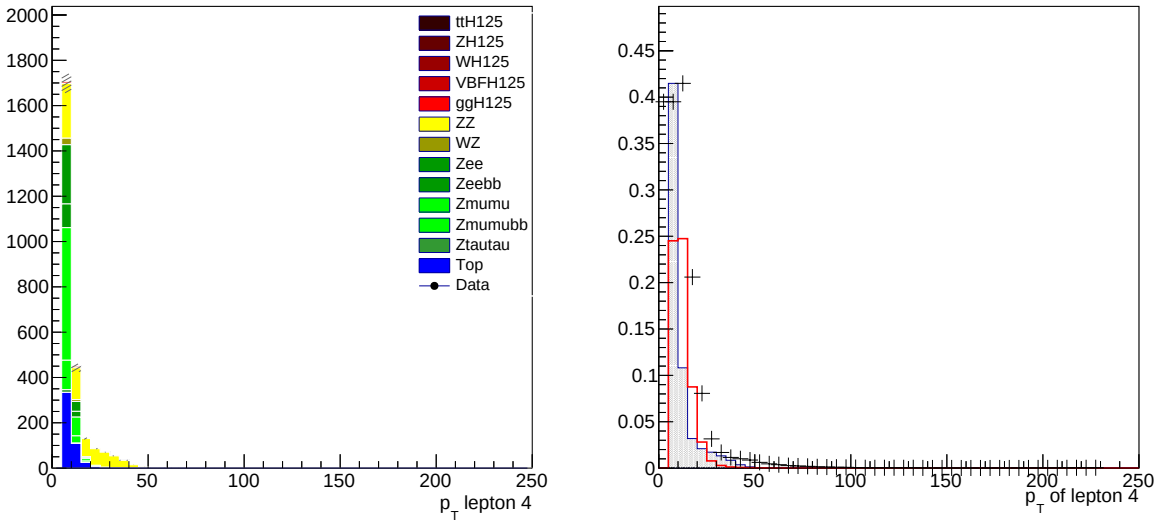

(a) transverse momentum of lepton 4 (b) upper cut of lepton 4

Figure 5.3: Histogram of the transverse momentum of lepton 4 together with its lower cut

Calorimeter Isolation

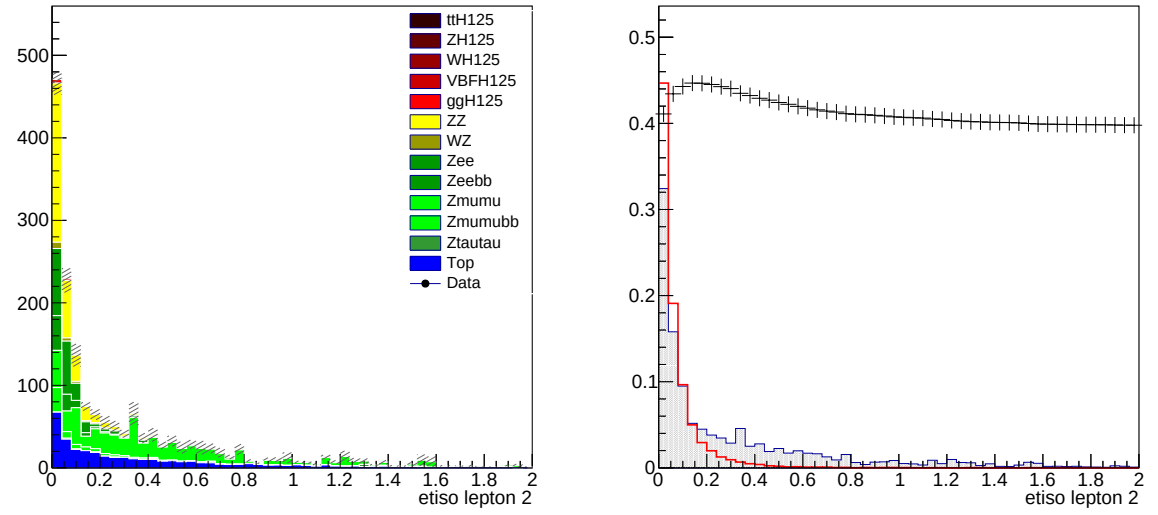

(a) calorimeter isolation of lepton 2 (b) upper cut of lepton 2

Figure 5.4: Histogram of the calorimeter isolation of lepton 2 together with the upper cut histogram

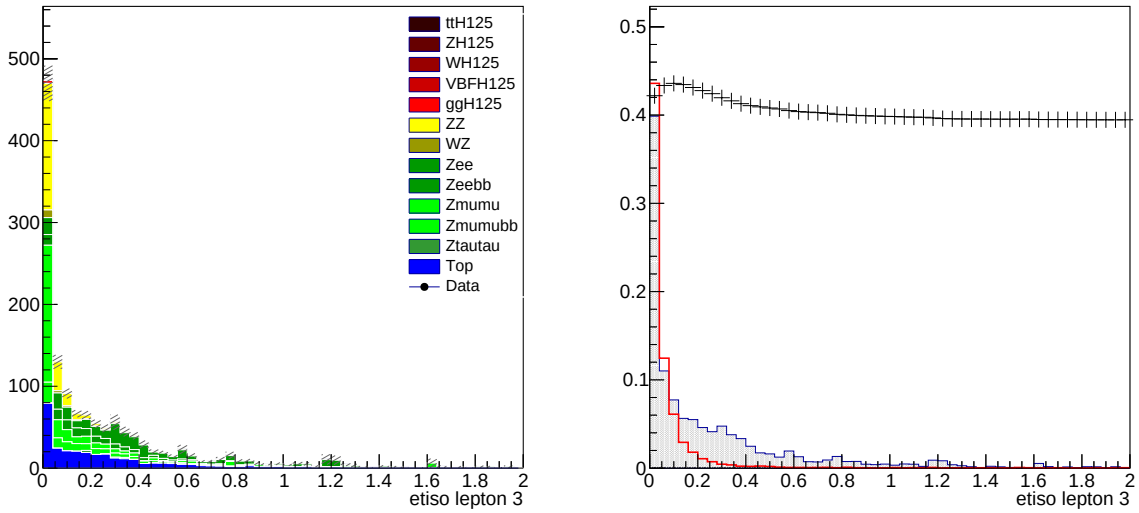

(a) calorimeter isolation of lepton 3 (b) upper cut of lepton 3

Figure 5.5: Histogram of the calorimeter isolation of lepton 3 together with the upper cut histogram

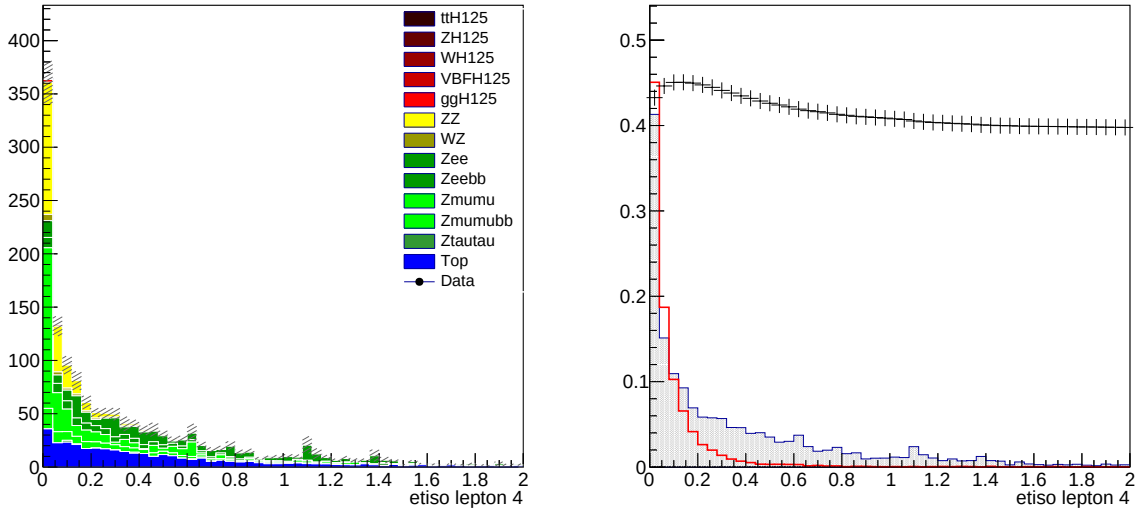

(a) calorimeter isolation of lepton 4 (b) upper cut of lepton 4

Figure 5.6: Histogram of the calorimeter isolation of lepton 4 together with the upper cut histogram

impact parameter significance $\frac{d_0}{\sigma_{d_0}}$

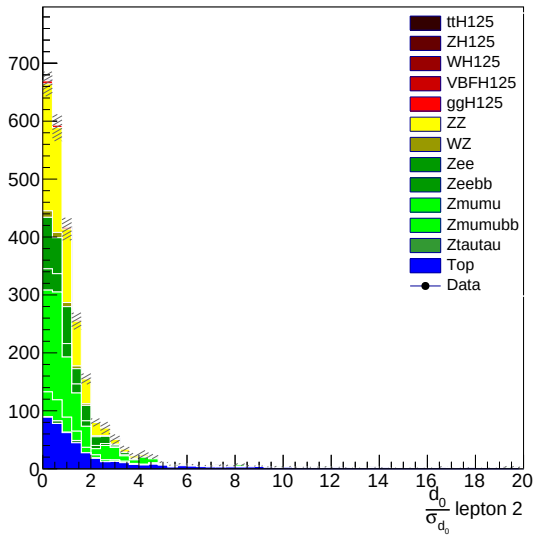

(a) impact parameter significance of lepton 2

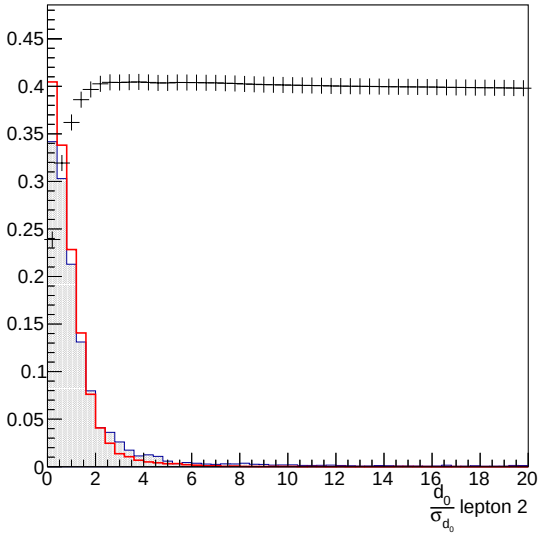

(b) upper cut of lepton 2

Figure 5.7: Histogram of the impact parameter significance with the upper cut histogram for lepton 2

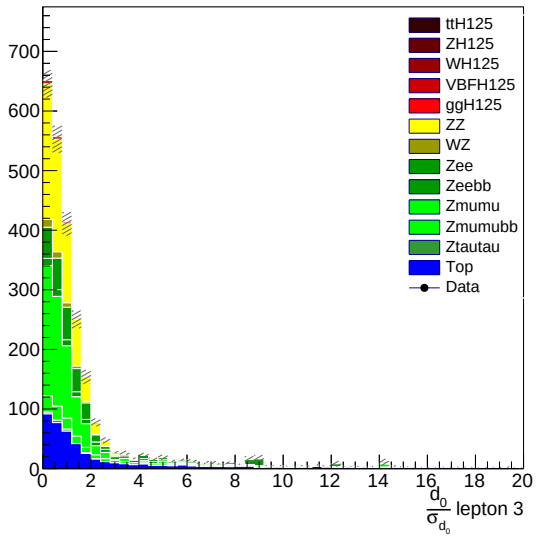

(a) impact parameter significance of lepton 3

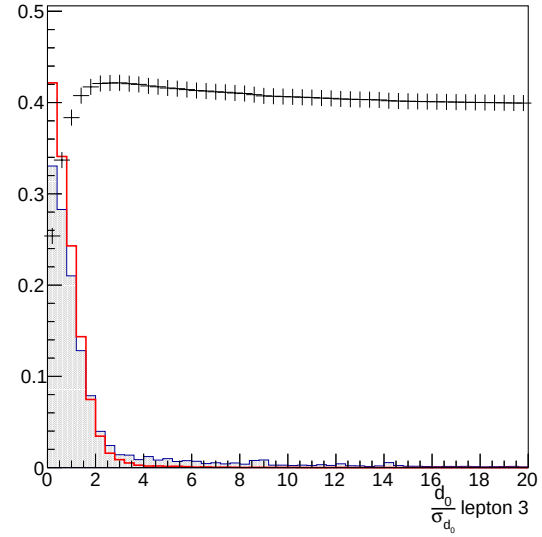

(b) upper cut of lepton 3

Figure 5.8: Histogram of the impact parameter significance with the upper cut histogram for lepton 3

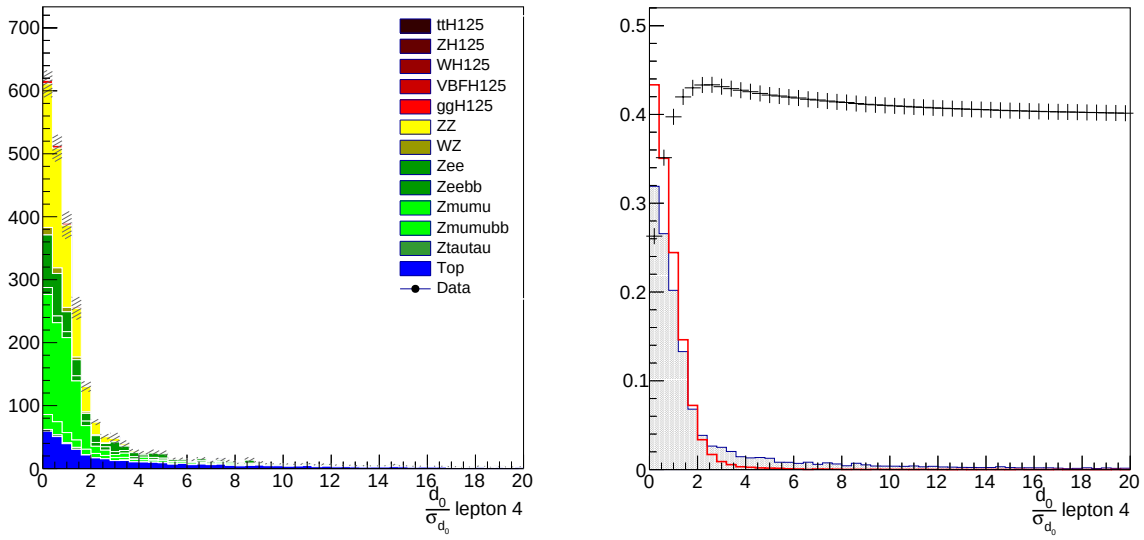

(a) impact parameter significance of lepton 4

(b) upper cut of lepton 4

Figure 5.9: Histogram of the impact parameter significance with the upper cut histogram for lepton 4

References

[1] The ATLAS collaboration: *Observation of a New Particle in the Search for the Standard Model Higgs Boson with the ATLAS Detector at the LHC*. Phys.Lett. B716 (2012) 1-29. arXiv:1207.7214

[2] Peter W. Higgs: *Broken Symmetries and the masses of Gauge Bosons*. Physical Review Letters Volume 13, Number 16, 1964. DOI:10.1103/PhysRevLett.13.508.

[3] Instructions Advanced Laboratory Course II. *"Measurement of the W-Boson Mass and Discovery of the Higgs-Boson at the ATLAS Experiment"*. Status 02/2020.

[4] Taking a closer look at LHC. https://www.lhc-closer.es/taking_a_closer_look_at_lhc/0.momentum Status 01.05.20 21:10 MET

[5] H. Kolanski, N. Wermes: *Teilchendetektoren: Grundlagen und Anwendungen*. Springer-Verlag Berlin Heidelberg 2016. DOI:10.1007/978-3-662-45350-6 .

[6] ATLAS Collaboration. https://atlas.cern/discover/detector/inner-detector, Status 24.04.20, 12:57 MET

[7] Aaboud, M., Aad, G., Abbott, B. et al.: *Electron reconstruction and identification in the ATLAS experiment using the 2015 and 2016 LHC protonproton collision data at* $\sqrt{s} = 13\,\text{TeV}$, Eur. Phys. J. C 79, 639, 2019. DOI:10.1140/epjc/s10052-019-7140-6

[8] P. Vankov: *ATLAS Upgrade for the HL-LHC: meeting the challenges of a five-fold increase in collision rate*. DESY 2012. arXiv:1201.5469v1

[9] J. Ellis: *Higgs Physics*. 2013. Edited version by M. Mulders and G. Perez. 2015. DOI:10.5170/CERN-2015-004.117

[10] ETH Zurich, https://grab-group.ethz.ch/research/higgs-boson.html, Status 26.04.20, 11:21 MET

[11] G. Aad et al: *Electron performance measurements with the ATLAS detector using the 2010 LHC proton-proton collision data*. Eur. Phys. J., C72, 1909, 2012. arXiv:1110.3174

List of Figures

List of Tables